J. Fluid Mech. (2013), *vol.* 720, *pp.* 236–279.
doi:10.1017/jfm.2012.642

Structural organization of large and very large scales in turbulent pipe flow simulation

J. R. Baltzer[1], R. J. Adrian[1,†] and Xiaohua Wu[2]

[1]School for Engineering of Matter, Transport and Energy, Arizona State University, P.O. Box 876106, Tempe, AZ 85287-6106, USA

[2]Department of Mechanical Engineering, Royal Military College of Canada, Kingston, Ontario, Canada K7K 7B4

(Received 12 August 2012; revised 12 November 2012; accepted 20 December 2012; first published online 27 February 2013)

The physical structures of velocity are examined from a recent direct numerical simulation of fully developed incompressible turbulent pipe flow (Wu, Baltzer & Adrian, *J. Fluid Mech.*, vol. 698, 2012, pp. 235–281) at a Reynolds number of $Re_D = 24\,580$ (based on bulk velocity) and a Kármán number of $R^+ = 685$. In that work, the periodic domain length of 30 pipe radii R was found to be sufficient to examine long motions of negative streamwise velocity fluctuation that are commonly observed in wall-bounded turbulent flows and correspond to the large fractions of energy present at very long streamwise wavelengths ($\geqslant 3R$). In this paper we study how long motions are composed of smaller motions. We characterize the spatial arrangements of very large-scale motions (VLSMs) extending through the logarithmic layer and above, and we find that they possess dominant helix angles (azimuthal inclinations relative to streamwise) that are revealed by two- and three-dimensional two-point spatial correlations of velocity. The correlations also reveal that the shorter, large-scale motions (LSMs) that concatenate to comprise the VLSMs are themselves more streamwise aligned. We show that the largest VLSMs possess a form similar to roll cells centred above the logarithmic layer and that they appear to play an important role in organizing the flow, while themselves contributing only a minor fraction of the flow turbulent kinetic energy. The roll cell motions play an important role with the smaller scales of motion that are necessary to create the strong streamwise streaks of low-velocity fluctuation that characterize the flow.

Key words: turbulent boundary layers, turbulent flows

1. Introduction

Recent direct numerical simulation (DNS) of a turbulent pipe flow by Wu, Baltzer & Adrian (2012) has shown direct evidence, without the use of Taylor's hypothesis, that very large-scale motions (VLSMs) of wavelength greater than 3 pipe radii (R) contribute over 40 % of the streamwise turbulent energy, and greater than 30 % of the uv (streamwise-wall normal) shear stress in that flow. That study focused mainly on statistical aspects and energy spectra of the flow. The purpose of the present study is to determine the structure associated with the very long-scale motions. Measurements of large fractions of streamwise turbulent energy and shear stress associated with

† Email address for correspondence: rjadrian@asu.edu

VLSMs in pipe experiments (Kim & Adrian 1999; Guala, Hommema & Adrian 2006) have brought about discussion of the flows' structural aspects. Numerical simulations of pipe flow allow the opportunity to observe very long structures at high resolution and in three dimensions without the limitations of experiments, such as the effects of using Taylor's hypothesis, as discussed in Wu *et al.* (2012).

Based on premultiplied energy spectra from thermal anemometry measurements indicating two distinct peaks in turbulent pipe flows, Kim & Adrian (1999) identified the motions associated with the longer-wavelength peak as VLSMs. This peak occurs from roughly the top of the buffer layer to wall-normal heights of typically $y/R \approx 0.25$–0.4 in which the peak wavelengths exceed three pipe radii and typically extend up to $14R$ (Kim & Adrian 1999). Kim & Adrian (1999) conjectured that VLSMs were a consequence of spatial coherence in the positions of hairpin packets. Evidence of hairpin packets, coherent organizations of streamwise-aligned hairpin vortices that grew as ramps with downstream position and were associated with uniform momentum zones of low streamwise velocity beneath them, was then emerging in wall-bounded shear flows based on studies of turbulent boundary layers (Adrian, Meinhart & Tomkins 2000) and channels (Zhou *et al.* 1999). Kim & Adrian (1999) associated the largest hairpin packets with bulges commonly observed in boundary layers, which had streamwise lengths of the order of the shorter-wavelength peak observed in the spectrum that was identified as corresponding to large-scale motions (LSMs). Thus, in this concept, hairpins organized into packets and packets aligned in a streamwise sense to establish VLSMs. Additional eddy types beyond packets were not needed to explain the wide range of long length scales observed in the spectra, although the mechanism by which alignment occurred was left as an open question, which could involve another flow mechanism. Further evidence for the concatenated packet model appeared in Guala *et al.* (2006) in a smoke wire visualization photograph from the pipe flow of Lekakis (1988) that showed smoke wavering azimuthally with a streamwise wavelength somewhat greater than $2R$. A photograph viewing the side reveals two distinct regions containing groups of wall-normal-inclined structures consistent with the presence of hairpins (as postulated in Adrian *et al.* 2000).

The VLSMs observed in pipes appear similar to those observed in channels, which are believed to contain structural elements similar to those of boundary layers. Balakumar & Adrian (2007) extended the pipe flow studies of Kim & Adrian (1999) and Guala *et al.* (2006) to boundary layer and channel flows and demonstrated the presence of LSM and VLSM indications in hot-wire spectra. Turbulent boundary layer and channel flows have generally received greater attention than pipes for studying structure. Besides the hairpin packet structure observed in boundary layers (Adrian *et al.* 2000), the study of Hutchins & Marusic (2007*a*) brought attention to the streamwise velocity structure of very long motions (which they termed 'superstructures') that scale in outer units and exist through the logarithmic region. With hot-wire rake measurements in laboratory boundary layers and a spanwise array of sonic anemometers in an atmospheric boundary layer, both of which required the use of Taylor's hypothesis, Hutchins & Marusic (2007*a*) confirmed that the log layers of these flows are populated with very long meandering features with lengths over 20δ (boundary layer thicknesses). Using turbulent channel DNS at $Re_\tau = 934$, they also found that superstructures extend as 'footprints' down to the near-wall region. They suggested that these structures may also be the VLSMs observed in pipe flows, but with structures in internal geometries having less meandering than in turbulent boundary layers, leading to longer length scales observed in the internal geometries.

Monty *et al.* (2007) extended the boundary layer study of Hutchins & Marusic (2007*a*) to channels and pipes using hot-wire rakes. They studied the spanwise or azimuthal correlation of streamwise velocity and the scale growth indicated by this quantity as wall-normal position increases. Their hot-wire traces using Taylor's hypothesis indicated that long, meandering low-speed regions flanked by high-speed regions in the spanwise or azimuthal direction were also present in the logarithmic regions of channels and pipes. They found that the logarithmic layers of turbulent boundary layers, pipes and channels have qualitatively similar structures.

Recently, several experimental studies have examined the structure in turbulent pipe flows. Bailey *et al.* (2008) and Bailey & Smits (2010) focused on interpreting structure based on two-point correlations calculated from spectra measured with a pair of hot-wire probes positioned for various azimuthal arclength separations (Δs) and radial positions. They also inferred streamwise scales by applying Taylor's hypothesis. Based on studying the behaviours of azimuthal width scales for LSMs and VLSMs as a function of wall-normal position y, Bailey *et al.* (2008) suggested that, if the VLSMs were created by streamwise alignment of hairpin packets (as suggested by Kim & Adrian 1999), only the oldest and largest hairpin packets align to create VLSMs. This is consistent with the Kim & Adrian (1999) concept of $2R$-long LSMs aligning and other evidence that the $2R$-long bulges are the largest packets. Bailey *et al.* (2008) also noted that the different azimuthal scales suggest the possibility that LSMs and VLSMs could be independent entities, with VLSMs possibly arising from linear or nonlinear instabilities.

Correlations similarly obtained for the same pipe flow configuration at $Re_D = 1.5 \times 10^5$ were used by Bailey & Smits (2010) to calculate azimuthal correlation contributions corresponding to motions with VLSM and LSM streamwise wavelengths and to generate proper orthogonal decomposition (POD) modes. In general, the radial–azimuthal correlations $R_{uu}(r, r', \Delta\theta)$ (with streamwise separation $\Delta x = 0$) had substantial magnitudes for less than about half the pipe circumference based on correlation contour plots, with the strong positive correlation near the reference probe position azimuthally surrounded by regions of negative correlation symmetrically located on either side. Bailey & Smits (2010) noted that this lack of correlation for $|\Delta\theta| > 90°$ suggests 'minimal interactions occur between motions on opposite sides of the pipe'. By decomposing the radial–azimuthal correlations at $\Delta x = 0$ into the contributions associated with VLSM and LSM streamwise wavelengths, they found that the VLSMs contribute much to the correlations at larger azimuthal angles from the reference position, whereas LSMs are generally associated with much of the positive correlation at narrower $\Delta\theta$ values. For reference wall-normal y values ranging from $0.1R$ to $0.5R$, the correlations associated with VLSMs at $\Delta x = 0$ indicated that velocity fluctuations in these positions remained correlated with points near the wall. Conversely, correlations associated with LSMs indicated motions for similar reference positions at sizable distances above the wall generally did not extend near the wall. They termed these LSM motions 'detached' and distinguished types of LSMs in this manner. Bailey & Smits (2010) suggested that the sizable difference in scales between correlations associated with LSMs and VLSMs for reference probe locations near the wall supports the idea of Bailey *et al.* (2008) that VLSMs may not be simply alignments of LSMs that occur near the wall. They also noted that the more similar scales between VLSMs and LSMs further from the wall could mean that VLSMs spanning from near the wall to high above form from alignments of detached LSMs located far above the wall. By performing POD, they observed a lack of clear delineation between eigenspectra associated with VLSMs and LSMs

and concluded that the two motions are interrelated. They also noted the possibility of a linear mechanism creating travelling waves similar to those observed in pipe transition (Eckhardt *et al.* 2007), but cautioned that more evidence would be necessary to support the existence of similar mechanisms, as there are a number of notable differences between transition and this fully turbulent regime.

POD calculations from experimental measurements of pipe flow were also performed by Hellström, Sinha & Smits (2011). Instead of hot-wire probes, they used particle image velocimetry (PIV) to approximate three-dimensional volumes by capturing velocity vectors in a radial–azimuthal plane and using Taylor's hypothesis. Focusing on a low-Reynolds-number ($Re_D = 12\,500$) turbulent pipe flow, they found that reconstructions with the 10 most energetic POD modes 'capture all the principal characteristics of the VLSM. This suggests that VLSMs are constructed of the most energetic POD modes that, when superimposed, give the impression of long meandering structures'. The most energetic POD modes shown consisted of straight, streamwise-aligned segments of positive and negative streamwise velocity fluctuation with various azimuthal widths. They also noted that 'the superposition of only the four most energetic modes will recreate meandering structures that appear to be much longer than any of its constituent modes'. Hellström *et al.* (2011) noted that these POD modes appeared similar to a sum of two helical response modes obtained from the linear stability analysis of McKeon & Sharma (2010), which calculated modes of a particular form that would experience maximum amplification in turbulent pipe flow. Hellström *et al.* (2011) found this to support the linear mechanisms associated with the existence of these propagating response modes proposed by McKeon & Sharma (2010).

Große & Westerweel (2011) used a similar PIV measurement technique to study the structures present in the pseudo-three-dimensional velocity fields, as well as various statistics, for turbulent pipe flows with Reynolds numbers ranging from $Re_D = 10\,000$ to 44 000. Their experiments also provided clear evidence of the very long structures of streamwise velocity. Große & Westerweel (2011) concluded that their measurements indicated the presence of low-speed and high-speed regions extending up to several pipe radii in streamwise length based on applying Taylor's hypothesis. They also observed these structures possessing strong coherence (i.e. similar shapes) for a wide range of radii ranging from $y/R = 0.05$ to 0.5. They computed probability densities of streak widths, which they found to be more strongly concentrated at short widths near the wall and more evenly distributed over a range of widths nearer the pipe core.

As noted above, the quasi-three-dimensional pipe fields obtained with radial–azimuthal PIV measurements rely on Taylor's hypothesis to infer the streamwise spatial variation from two-dimensional fields closely spaced in time. Significant differences can occur in the longest motions between instantaneous fields and those obtained by applying Taylor's hypothesis (Dennis & Nickels 2008; del Álamo & Jiménez 2009; Wu *et al.* 2012). In addition, this technique presents issues for measuring velocity in the region very near the wall. Hellström *et al.* (2011) discarded the $y/R < 0.1$ region because of optical refraction issues. Große & Westerweel (2011) found significant difference in velocity fluctuation statistics relative to DNS for $y/R < 0.1$ at their highest Reynolds number, probably as a result of insufficient resolution for this region in the experiment.

Given these experimental limitations, DNS data are particularly well suited to examining the structure of very large-scale motions without the use of Taylor's hypothesis while resolving the smallest relevant motions. Although structure has been observed in several previous pipe simulations performed at lower Reynolds

numbers (e.g. Eggels *et al.* 1994; Duggleby, Ball & Schwaenen 2009), relatively few have been performed for $Re_D > 10\,000$. Wu & Moin (2008) performed pipe simulations for $Re_D = 5300$ and 44 000 and generally focused on statistics but made several visualizations of streamwise velocity. At $Re_D = 44\,000$, they noted the presence of much 'fine-grain structure'. In a constant θ plane, they observed a 'large number of worm-like elongated high-momentum structures with very narrow azimuthal dimension'. The domain length of this simulation limited the study of very long structures.

The present DNS has a Reynolds number high enough to include significant energy at VLSM scales (wavelengths $\lambda_x \geqslant 3R$) and a domain length of $30R$ that is long enough for examination of very long structures, with attention given to how various smaller scales relate to the VLSMs that are significant in energy spectra. Although DNS is subject to numerical accuracy, computational domain size and streamwise periodicity issues, the present simulation has been verified by generally good agreement with experimental statistics (Wu *et al.* 2012).

This study characterizes the VLSMs in the pipe flow simulation, their relation to smaller structures, their organization and their similarities to experimental observations and structural concepts for wall-bounded turbulent shear flows. From energy spectra considerations, VLSMs are known to be very significant in the log-layer region (Guala *et al.* 2006; Hutchins & Marusic 2007*a*; Wu *et al.* 2012). The log layer is also theorized to contain self-similar structures (Perry & Chong 1982; Adrian *et al.* 2000; Marusic 2001), and therefore this region is of particular interest. However, the Reynolds number of the simulation limits the range of scale separation that is present, and in particular the separation between the near-wall region and the logarithmic layer.

The near-wall region is defined herein to be the flow region extending from the wall that is characterized by intense quasi-streamwise vortices concentrated near $y^+ = 20$, although the quasi-streamwise vortices extend upwards towards $y^+ = 60$ in Jeong *et al.* (1997). The near-wall region is recognized to contain very strong velocity fluctuations with high- and low-speed streaks (relative to the mean) in alternating spanwise (or azimuthal) arrangements with a consistent wavelength of $\Delta s^+ = 100$ (Kim, Kline & Reynolds 1971; Smith & Metzler 1983). The behaviour of the near-wall region has been extensively analysed (e.g. Aubry *et al.* 1988; Johansson, Alfredsson & Kim 1991; Jeong *et al.* 1997; Jiménez & Pinelli 1999; Schoppa & Hussain 2002). The near-wall region has been found to sustain itself autonomously, and the behaviour within the near-wall region is largely reproduced even when the flow above $y^+ \approx 60$ is artificially damped (Jiménez & Pinelli 1999). In an actual flow, motions extending to greater distances above the wall (including VLSMs) are known to have an influence in the near-wall region (Hutchins & Marusic 2007*a*).

In contrast to the motions characterizing the near-wall region, we focus on motions, including VLSMs, that are particularly pronounced in the log layer. We define the log layer in the classical sense based on the mean velocity profile, and $y^+ = 30$ to $y/R = 0.15$ is taken as the nominal range of the log layer (Marusic & Adrian 2013). The significant interaction between the near-wall region and the lower extent of the log layer has led some researchers to suggest larger y^+ values for the beginning of the log layer (e.g. del Álamo *et al.* 2006). Shear-layer structures of strong azimuthal vorticity originating in the near-wall region (Johansson *et al.* 1991) extend into the log layer when it is defined with a lower limit of $y^+ = 30$. Therefore, we focus attention onto the highest extent of the log layer, $y/R = 0.15$, where the most direct influence of the near-wall motions (as defined by the quasi-streamwise vortical structures) is expected to be relatively minimal. In the present pipe flow, $y/R = 0.15$ corresponds to $y^+ = 101$.

Townsend (1976) postulated that, in the context of log layers, the velocity at a specific location is principally due to the effects of vortical structures (eddies) extending to higher locations above the wall, suggesting that, for the $y^+ = 101$ location of interest in the present flow, the direct effects of the near-wall vortices would be smaller than the contributions from taller structures.

In this study, we first visualize the velocity streaks in a streamwise–azimuthal cylindrical surface located near the upper extent of the log layer, describe their characteristics, and statistically quantify their lengths (§ 3). Next, we visualize the velocity structures' radial extents (§ 4) to reveal the near-wall footprints attached to low-momentum regions. We then employ conditional averages to study the overall organization pattern of the very long streamwise velocity fluctuation streaks (§ 5). Finally, we explore the patterns of the other velocity components associated with the streamwise velocity fluctuation streaks (§ 6).

2. Computational details

In the present study, the unit length scale is pipe radius R, and the unit velocity scale is U_{bulk}, which is defined as the ratio of mean volume flow rate and pipe cross-sectional area. The unit time scale is therefore R/U_{bulk}. The Reynolds number based on pipe diameter D and U_{bulk} is $Re_D = 24\,580$, and the Kármán number is $R^+ = 685$. An overbar denotes ensemble averaging, and a superscript $+$ refers to quantities normalized by friction velocity u_τ for velocity and by viscous wall unit ν/u_τ for distance. Additional details of the simulation and its validation are described in Wu *et al.* (2012).

The radial coordinate r is measured from the pipe axis, x is the flow axial direction, and θ is the azimuthal coordinate. For the purpose of analogy with the spanwise coordinate of a channel, we introduce the arclength $s = r\theta$. (The use of arclength in turbulent pipe flows is discussed by Monty *et al.* (2007).) By analogy with the wall-normal coordinate of a channel, it is also convenient to define $y = R - r$ for the pipe (also used by Guala *et al.* 2006). It is also helpful to introduce the analogous velocity components $u = u_x$, $v = -u_r$ and $w = u_\theta$. The subscripts of the correlation functions herein use u, v, w to indicate the velocity components. An overbar represents averaging over time as well as over the two homogeneous directions. Prime symbols (e.g. u') are used to represent fluctuating quantities from Reynolds decomposition.

3. Long streaks of streamwise velocity fluctuation

As noted in the introduction, long streaks of streamwise velocity (u) fluctuation are ubiquitous in canonical wall-bounded shear flows. A cylinder at $y/R = 0.15$ and $y^+ = 101$, towards the top of the log layer, is clearly visualized when rolled out to be viewed as a plane (Monty *et al.* 2007) and is analogous to constant y planes viewed in channel and boundary layer flows. Contours of streamwise velocity fluctuation at an instant in time (figure 1) appear qualitatively similar to those obtained from pipe experiments using Taylor's hypothesis (Monty *et al.* 2007; Große & Westerweel 2011; Hellström *et al.* 2011), with long, approximately streamwise-oriented, streaks of low- and high-velocity fluctuations visually dominant. The appearance of the low-velocity streaks is similar to that at $y/R = 0.10$ in the $Re_D = 44\,000$ pipe flow of Große & Westerweel (2011). Qualitatively, the behaviour contains meandering with frequent 'joining and splitting of streaks' that they observed at a location yet nearer the wall. At radii relatively near the wall (not deep within the core of the pipe), Große & Westerweel (2011) observed that streaks do not persist across the

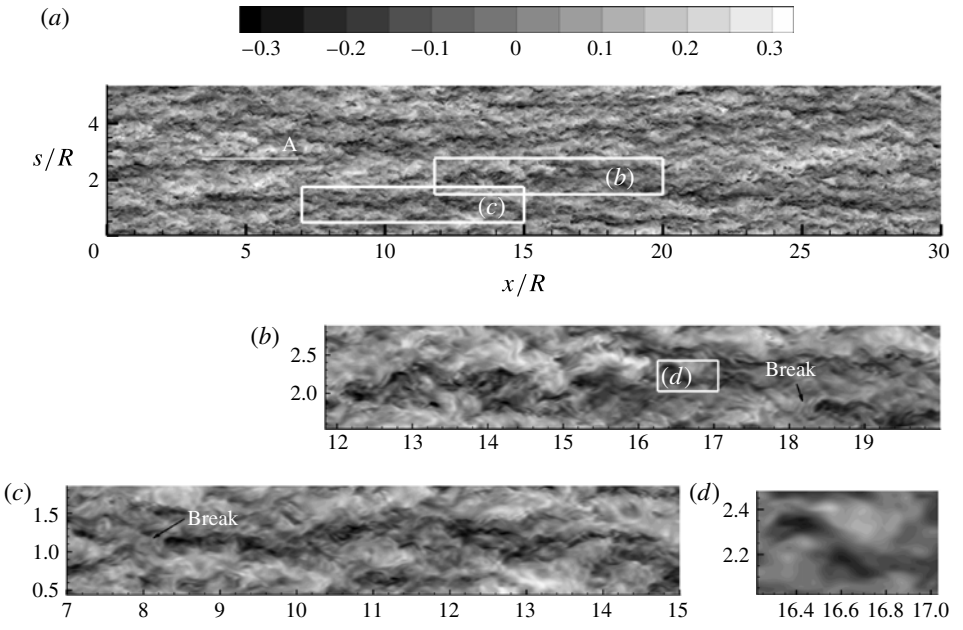

FIGURE 1. Axial velocity fluctuation u'/U_{bulk} contours of a streamwise–azimuthal cylinder at $t = 252R/U_{bulk}$ and radius where $y/R = 0.15$ and $y^+ = 101$. (*a*) The entire simulation domain; (*b*,*c*) two prominent long, streaky, low-speed regions shown in greater detail; (*d*) even finer detail of a very fine-scaled motion. A relatively straight low-speed streak in panel (*a*) is identified as A for further visualization.

centreline (i.e. do not travel azimuthally by 180°), and the streaks in the present DNS behave similarly. Monty *et al.* (2007) observed several examples of low-speed streaks travelling 180° around the circumference at $y/R = 0.15$, but these were at significantly higher Reynolds number ($Re_\tau = 3472$ and $Re_D = 152\,000$). The limited azimuthal resolution of the hot-wire rake may also have made discerning individual streaks more difficult. The domain of the present simulation, for which an unwrapped constant-radius cylinder is shown in figure 1(*a*), includes a number of long negative u' streaks. The multiple scales of motion with varying strengths and unclarity with respect to which motions are connected lead to ambiguity with regard to where each streak begins and ends.

Two examples of low-speed streaks are shown in greater detail in figure 1(*b*,*c*). The presence of multiple scales of motion, with many fine-scale turbulent fluctuations, is clear. However, more distinct upstream and downstream breaks in a connected organization of low-momentum fluctuations become apparent when viewed at this higher resolution. The left and right boundaries of figure 1(*b*) correspond to the apparent breaks (ends of an approximately contiguous extent) in long streamwise motions. In this panel, there appears to be a long low-speed motion between $x/R = 12$ and 18 and another at greater s/R (azimuthal location) between $x/R = 15$ and 20. The break identified near $x/R = 18$ is much clearer and marks the beginning of a low-speed motion that extends far past the panel. Both figure 1(*b*,*c*) contain low-speed regions that appear to be wavering in an azimuthal sense. Hutchins & Marusic (2007*a*) observed wavering in the logarithmic layers of other wall-bounded turbulent shear flows. By various means, we seek to characterize the streak patterns and their

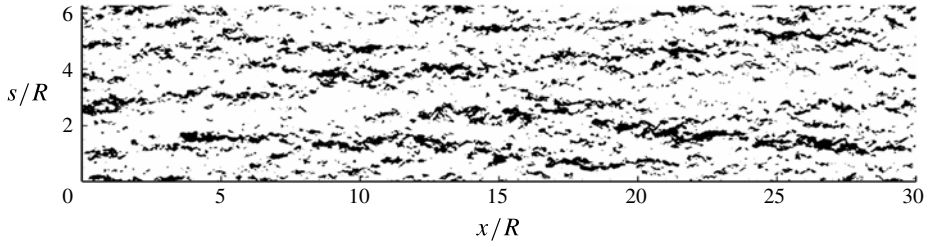

FIGURE 2. Axial velocity fluctuation contours of a streamwise–azimuthal cylinder at $t = 252R/U_{bulk}$ and radius where $y/R = 0.15$ and $y^+ = 101$ (also shown in figure 1*a*). Black regions are the regions of strong negative u' fluctuation with velocity below the contour threshold level of $u'_{thr}/U_{bulk} = -0.10$, which is approximately the r.m.s. fluctuation magnitude at this radius.

scales in the present pipe flow. In figure 1(*c*), within the overall streak, several of the strongest segments of negative fluctuation appear to be more streamwise-aligned, such as the regions from $x/R = 8.2$ to 9 and from $x/R = 12$ to 13. Viewing further detail of the small-scale fluctuations in figure 1(*d*), these smallest distinctive motions appear to consist of slightly streamwise elongated negative velocity fluctuation peaks that decay in magnitude rapidly with distance from the peak location. While this will be discussed in greater detail, the streak appears to be composed of these somewhat randomly oriented but similarly dimensioned small fluctuations, suggesting concatenations of small motions.

The multiple strengths of u' fluctuation in figure 1 indicate the ambiguity inherent in defining the streaks and calculating their lengths. One method of characterizing the lengths of the streaks is measuring the lengths of contiguous regions with velocity fluctuation below a threshold value, such that a structure that is contiguous but wavers (or is azimuthally inclined) is identified as a single structure. Based on quasi-three-dimensional velocity measurements in a turbulent boundary layer, Dennis & Nickels (2011) extracted isosurfaces of negative velocity fluctuation at a particular threshold value (10 % of the local mean velocity) and measured their streamwise lengths to create a histogram representing the frequencies at which they exist. Große & Westerweel (2011) calculated histograms of azimuthal widths of velocity structures, and found that introducing a threshold was also necessary.

For the present study of structures' streamwise lengths, clusters of points with velocity fluctuations below a specified fraction of the bulk velocity are extracted from a streamwise–azimuthal plane, and the streamwise lengths of the resulting point clusters are statistically quantified. To illustrate the contiguous regions identified for the same region as that shown in figure 1(*a*), filled contours of negative fluctuations stronger than a threshold value u'_{thr} of $-0.10U_{bulk}$ are displayed in figure 2. Overall, these contours create the visual impression of scattered strong small-scale negative fluctuations, with some touching and forming longer contiguous regions, others almost touching but forming shorter contiguous regions, and many small-scale negative fluctuations scattered and disconnected but often organized along streak-like lines. This suggests that what comprises a streak is significantly dependent on the threshold value chosen, if a streak is defined in this manner. More significantly, figure 2 suggests a clear very large-scale organizing tendency that is explored by other means in §§ 5 and 6.

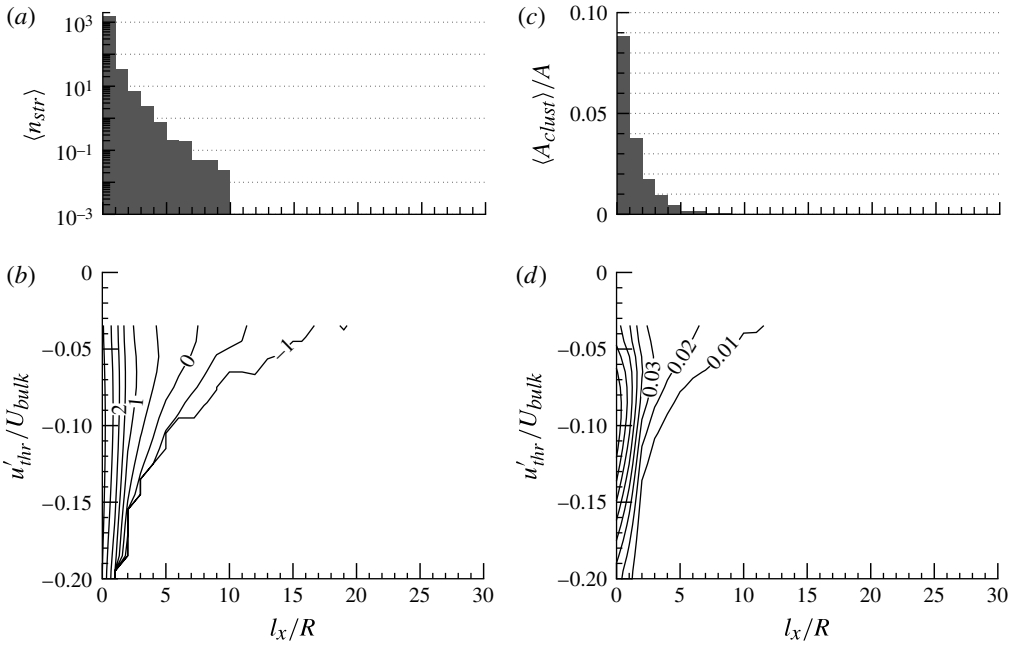

FIGURE 3. Histograms of streamwise length of contiguous regions of negative u' fluctuation stronger than a threshold for the streamwise–azimuthal cylinder surface at $y/R = 0.15$ ($y^+ = 101$). (*a*,*b*) The mean number of such structures with the specified length range per field; (*c*,*d*) the mean area contributed by these structures per field. For panels (*a*,*c*), the threshold value is $u'_{thr} = -0.10U_{bulk}$. Panel (*b*) contains contour lines of $\log(\langle n_{str}\rangle)$ and panel (*d*) contains contour lines of $\langle A_{clust}\rangle/A$, where A_{clust} is the area occupied by the clusters in the specified bin and A is the total area of the streamwise–azimuthal cylinder surface.

Histograms of the corresponding low-speed streak lengths are presented for $y/R = 0.15$ in figure 3 with the same contour threshold level of $u'_{thr}/U_{bulk} = -0.10$ for which contours are shown in the example field of figure 2. Contiguous structures are allowed to cross the periodic boundaries of the domain. The frequencies of occurrence are counted for bins encompassing ranges of one pipe radius in streamwise length. The mean number of structures with streamwise lengths that fall within each bin per field is displayed in figure 3(*a*). Every streamwise length is included, and the shorter structures occur much more frequently than longer ones, so the vertical axis is displayed on a logarithmic scale. Clearly, the vast majority of contiguous low-speed regions for this threshold value have streamwise lengths less than R. As $\langle n_{str}\rangle = 1$ indicates that an average of one structure within the corresponding bin occurs per instantaneous x–θ cylinder, the histogram indicates that only structures with lengths less than $4R$ occur more than once per field at $y/R = 0.15$, on average, for this threshold. In general, the results for the present pipe are broadly similar to those for the boundary layer experiment of Dennis & Nickels (2011) and support the same trends given the differences in flow and algorithm, with less than 5 % of extracted structures being longer than $7\{R, \delta\}$ in both cases.

While the results demonstrate that the lengths are subjective with respect to the choice of threshold value, the length distributions change gradually. Dennis & Nickels (2011) noted that 'changing the level within a reasonable margin does not alter the

distribution greatly', although their algorithm differed by measuring three-dimensional structures. To address the effect of threshold, figure 3(*b*) includes contour lines of $\langle n_{str} \rangle$ histogram values (logarithmically spaced) for structure length bins also as a function of threshold value. Thus, figure 3(*a*) is a bar chart representation of the horizontal slice of figure 3(*b*) at which $u'_{thr}/U_{bulk} = -0.10$. In general, the occurrence frequencies of the longest structures are most sensitive (in terms of per cent change) to the threshold values. The length bin for which $\langle n_{str} \rangle = 10^1$, for example, remains much more constant with changing threshold, and is at approximately $l_x/R = 3$ in the vicinity of the threshold noted above, so contiguous streaks of length $3R$ and shorter generally exist most frequently, with several longer streaks also likely per field.

In the context of a different quantity (relating to vortical motions), del Álamo *et al.* (2006) discussed the phenomenon of the clusters of connected points satisfying a selected threshold merging into a few complex, confusing objects as the threshold value is reduced. In figure 3(*b*), the contour lines representing the $\langle n_{str} \rangle$ values of 10^1 and 10^2 peak at longer structure lengths as threshold magnitude is reduced. For high threshold magnitudes, as the threshold magnitude is reduced, more and more contiguous regions of negative fluctuation appear and other regions that existed at stronger threshold connect to form longer regions. The contour line peaks in figure 3 occur when the threshold favours contiguous regions with lengths of R to $3R$, but the regions of such lengths begin to coalesce together for further reduction of the threshold value. For the longest length bins, the dominant source for the creation of such structures with decreasing threshold strength is the combining of shorter structures (as opposed to individual regions gradually lengthening), and the occurrence frequency of such structures monotonically increases with decreasing threshold magnitude. Statistics are not calculated for threshold magnitudes that are too small because the extracted structures begin to span the entire periodic domain and are difficult to interpret.

Although relatively small numbers of long structures ($l_x > R$) are extracted, this statistic does not directly represent their importance, such as their contribution to turbulent kinetic energy. Owing to the longer structures' greater areas in the $y/R = 0.15$ surface, each such structure occupies a larger fraction of the domain than each short-length structure. For this reason, the fraction of the x–θ cylindrical surface area occupied by clusters within each length bin ($\langle A_{clust} \rangle / A$) is also calculated. The mean area fractions are presented on a linear scale in figure 3(*c*) and with linearly spaced contour levels in figure 3(*d*), whereas the mean frequencies of occurrence are presented logarithmically. Since each bar in figure 3(*c*) indicates the mean area fraction that low-speed streaks of each contiguous length at the selected threshold contributes, the sum of all bars is the total fraction of the area occupied by regions of negative fluctuations stronger than the threshold value ($u' < u'_{thr}$).

While this is one method of characterizing the low-speed structure lengths, the most common statistical indications of structure lengths in turbulent flows are energy spectra. It is on this basis that VLSMs are traditionally defined as motions with streamwise Fourier wavelengths of $3R$ and greater ($\lambda_x \geqslant 3R$) (Guala *et al.* 2006). The energy spectra for the present pipe simulation in Wu *et al.* (2012) indicate that the flow contains a significant fraction of u energy in the VLSM streamwise wavelengths, with approximately 44 % of the energy associated with $\lambda_x \geqslant 3R$ when averaged over all radii. While experimental pipe spectra in the logarithmic layer at sufficiently high Reynolds number formed a distinct peak at long wavelength that corresponded to the VLSMs and led to the spectrum appearing in a bimodal form (Kim & Adrian 1999), at least some of this peak is introduced by error due to applying Taylor's hypothesis for

the experiments (del Álamo & Jiménez 2009). Although this region of the spectrum is flatter in DNS for which true spatial spectra are calculated and more consistent with a theoretical k_x^{-1} behaviour at long wavelengths (del Álamo & Jiménez 2009), Wu *et al.* (2012) found that a very weak peak may possibly be forming (with a much higher-Reynolds-number DNS necessary to definitively determine if this is the case). In any case, the spectrum was reasonably represented with a bimodal form.

The issue remains of how the distribution of energetic wavelengths represented by the spectra is related to the distribution of scales revealed by the contiguous low-speed region extraction algorithm described above. Since Fourier wavelengths represent the wavelengths of periodicity, they involve both positive and negative fluctuations arranged in a streamwise periodically alternating fashion. It is reasonable that the strongest Fourier wavelengths would be associated with this period relatively independently of the exact form of the fluctuation, and additional Fourier components would assume a less dominant role. This is suggested by the example of the Fourier series representations of a square wave and triangular wave in which the dominant wavelengths are those of the periodic signal in each case. If one considers a negative fluctuation of a certain length immediately neighbouring, in a streamwise sense, a positive fluctuation, then the dominant wavelength would be twice the length of the negative structure. This assumes that the lengths of positive and negative fluctuation structures are the same. In boundary layers, the distribution of high-speed fluctuation streaks is relatively similar to that of their low-speed counterparts, but somewhat weighted towards shorter streamwise extent, according to the results of Dennis & Nickels (2011).

In the present pipe flow's premultiplied energy spectrum (Wu *et al.* 2012), the energy in the logarithmic layer region begins to decay rapidly with increasing wavelength at approximately $\lambda_x = 10R$, which suggests (in the previously discussed scenario) the presence of periodically occurring low-velocity structures of length $5R$. The statistics of extracted structures in figure 3(*c*) indicate that the areas occupied by contiguous low-speed fluctuation decrease to relatively small values for structures longer than approximately $5R$ at that threshold value. The complexity of structure organization also complicates the link between the energy spectra and extracted low-speed structures. The statistics of extracted structures generally support the importance of structures with lengths corresponding to VLSMs, although the structures extracted for the strongest negative fluctuations are clearly of small scale, with evidence that they spatially organize. Organization and wavering of structures also clearly affects their associated energy spectra, as explored in depth by Hutchins & Marusic (2007*a*). They showed that a relatively simple streak produces energy at a range of length scales and the distribution is affected by meandering. Therefore, additional aspects of the structure dimensions and the organization of structures are considered next.

4. Radial extent of velocity structures

While the velocity fluctuations shown in figure 1 are for $y/R = 0.15$ ($y^+ = 101$), near the top of the logarithmic region, the radial extent of the low-speed structures is significant. In a turbulent channel simulation, Hutchins & Marusic (2007*a*) noted that the 'footprints' of streamwise velocity extend down to very near the wall. In turbulent pipe flow, the correlations of Bailey & Smits (2010) suggest that VLSMs remain well correlated down to the pipe wall. The example pipe field in figure 4 demonstrates the correlation between streamwise velocity fluctuations (u') between various radii.

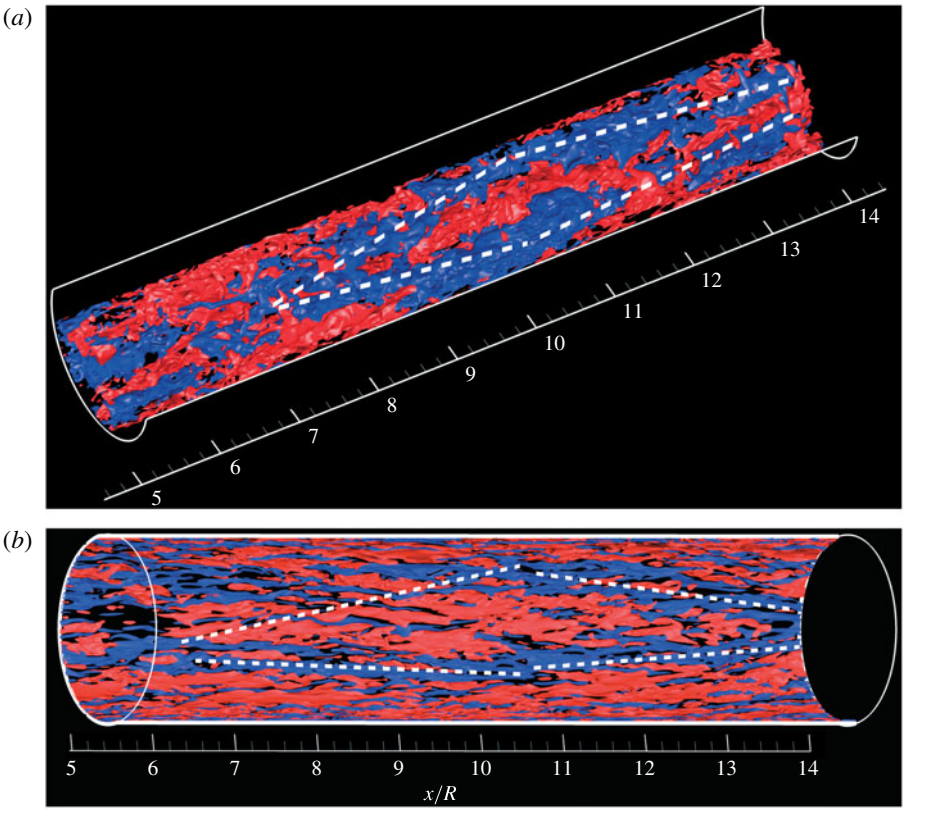

FIGURE 4. Example streamwise velocity fluctuations at $t = 324R/U_{bulk}$ visualized by isosurfaces of $u' = -0.1U_{bulk}$ (blue) and $0.1U_{bulk}$ (red). The radial sections included are (*a*) $30 < y^+ < 685$ and (*b*) $y^+ < 30$.

Owing to the strong differences in behaviour between the near-wall region and the flow more distant from the wall, the domain section is split at $y^+ = 30$, which is the division between the buffer and log layers. The region below $y^+ = 30$ contains the majority of the near-wall quasi-streamwise vortices and the strongest streamwise velocity fluctuations. The pipe section is cut in half radially (cut along a constant θ), and streamwise velocity fluctuation is visualized by colour isosurfaces at strengths of $\pm 0.1U_{bulk}$. In figure 4(*a*), the isosurfaces extend through the logarithmic layer and above, with a consistent pattern spanning the radii. For clarity, some of the θ is omitted. Planes extracted and flattened from a series of radii in this region reveal a unique diamond shape of low-speed fluctuations in this particular section. This shape can be explained as a superposition of relatively straight but azimuthally inclined low-speed regions that are further described in § 5.4. The diamond arrangement, drawn in figure 4 with dashed lines, does not appear to occur particularly frequently, but is a distinct pattern to observe for the present purpose. A cylindrical surface of the velocity at $y/R = 0.39$ ($y^+ = 270$) reveals that elements of the diamond pattern remain discernible, suggesting that structures of streamwise velocity motions often extend over significant fractions of R, through the log layer and above. Statistical correlation will be shown to support the large radial extents of such motions.

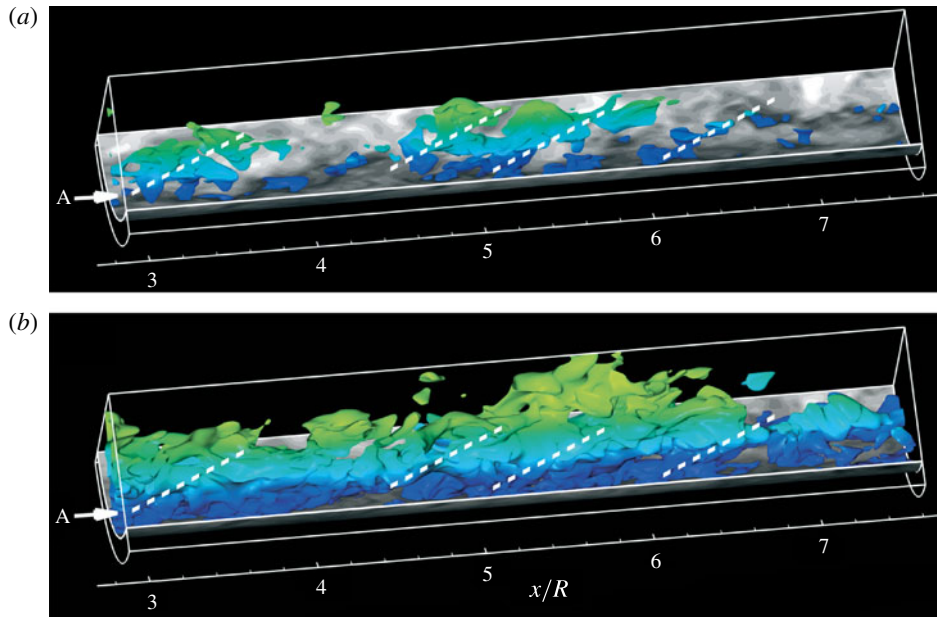

FIGURE 5. Three-dimensional isosurfaces of negative u fluctuation for the pipe section containing low-speed streak A in figure 1 ($t = 252R/U_{bulk}$). The cylinder shown in figure 1 at $y/R = 0.15$ with grey contours is included. The isosurfaces are coloured according to radius, ranging from blue nearer the pipe wall to green at the centreline. Isosurfaces of u' are visualized for values of (*a*) $-0.2U_{bulk}$ and (*b*) $-0.1U_{bulk}$.

The region within $y^+ = 30$ of the wall in figure 1 also retains evidence of the diamond pattern identified at greater y values, consistent with VLSM footprints extending near the wall (Hutchins & Marusic 2007*a*). The greater strength of the fluctuations in this region relative to the constant isosurface value leads to dense population with isosurfaces. The fine scales present in this region can be attributed to the near-wall motions previously noted. The characteristic azimuthal widths of near-wall low-speed streaks ($\Delta s^+ \approx 100$) are visually notable and are associated with much of the turbulent kinetic energy content in this region.

Figure 5 depicts isosurfaces of negative streamwise velocity fluctuation with a weaker u'/U_{bulk} level than in figure 4, in order to emphasize the structures more distant from the wall. The region visualized is that of figure 1 in which low-speed streak A was identified. The $y/R = 0.15$ ($y^+ = 101$) surface of greyscale contours from figure 1 is included on figure 5. Only the region above this surface is visualized to clearly display the negative u' fluctuations at the top of the log law region and above. The isosurfaces highlight the negative velocity fluctuations penetrating far towards the pipe centreline.

Low- and high-velocity streaks may be visualized with isosurfaces representing fixed values of several possible quantities, including u' fluctuations scaled by the local root-mean-square (r.m.s.) fluctuation or local mean $\bar{u}(y)$, as suggested by Dennis & Nickels (2011). The present visualizations use u' normalized by U_{bulk}, a normalization that is independent of y. Relative to the present method, normalizing by the local mean would tend to emphasize the structures near the wall where the mean velocity is small and fluctuation intensities are large, whereas normalizing by the local r.m.s.

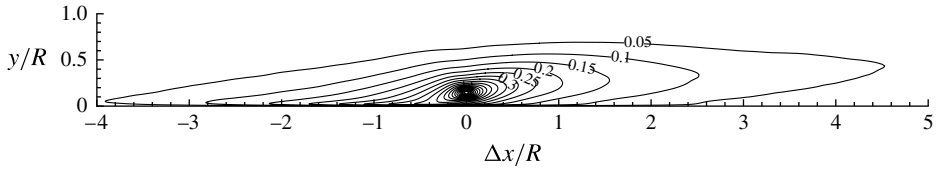

FIGURE 6. Contour lines of correlation coefficient R_{uu} indicating an estimate of the streamwise velocity fluctuation structure associated with a negative (or positive) u fluctuation at the event location ($\Delta x = 0$, $y = 0.15R$).

would strengthen motions far from the wall where intensity is weaker. In a turbulent boundary layer, Lee & Sung (2011) plotted isosurfaces of negative velocity at a specific value independent of wall-normal position. It should be recognized that fluctuations that weaken in accord with the lowering intensity in the core may persist significantly further from the wall than depicted in figure 5. A weaker constant threshold or appropriate radial scaling (e.g. by local r.m.s. velocity) would reveal such structures.

The long structures contained in figure 5 are typical of the negative velocity structures occupying the pipe. The visualizations indicate that the motions observed in the log-layer region penetrate deeply into the core, with the overall trend of ramp-like inclination indicated by the dashed lines for streak A. While the structures below approximately $y/R = 0.15$ have a strongly swept (inclined at a shallow wall-normal angle) appearance, probably due to the very strong shear in this region, the strong structures visualized above this wall-normal location in figure 5(*a*) appear to be inclined at a steeper wall-normal inclination (more similar to 45°). Further from the wall than $y/R = 0.15$ in this flow, the strong negative fluctuations appear more broken up than the continuous streak A visualized in figure 1, with the three-dimensional structures appearing like a concatenation. It should be noted that the isosurfaces at $u'/U_{bulk} = -0.2$ represent the stronger motions comprising the streak visible in the contours at $y/R = 0.15$. Visualizing the isosurface value of $-0.1U_{bulk}$ in figure 5(*b*) reveals a more continuous streak without the clear steep wall-normal inclinations of the stronger motions.

The statistically averaged properties of the structure associated with a velocity fluctuation at a reference height of $y = 0.15R$ are revealed by the two-point correlation in figure 6. The overall picture is that of an LSM consisting of a series of wall-normal-inclined negative velocity regions. In terms of overall dimensions and organizations, the negative u' motions are generally consistent with the low-speed regions that occur under the heads of hairpin vortices as described in other studies (e.g. Adrian *et al.* 2000). The ramp-like character of the u' two-point correlation is consistent with those of turbulent boundary layers (e.g. Hutchins & Marusic 2007*a*) in which hairpins are experimentally established (e.g. Adrian *et al.* 2000). The linear stochastic estimate (LSE) of the velocity field given a swirling strength event used to specify the head of a hairpin (not shown for this flow) is also consistent with that of channel flow interpreted in light of hairpin packets (Christensen & Adrian 2001). The aligned collection of low-speed regions is consistent with a packet of hairpins having a height of the order of one pipe radius and length of the order of one to three pipe radii. This interpretation is supported by the patterns of motion found in the streamwise–radial planes of a large number of realizations (Baltzer 2012) that coincide with the patterns found in PIV measurements by a number of investigators (Adrian

et al. 2000; Ganapathisubramani, Longmire & Marusic 2003; Tomkins & Adrian 2003; Hutchins, Hambleton & Marusic 2005; Hambleton, Hutchins & Marusic 2006; Wu & Christensen 2006; Volino, Schultz & Flack 2007).

Definitive identification of the large-scale motions as mature hairpin packets requires visualization of the three-dimensional hairpin vortices surrounding the low-momentum regions in many realizations such as that in figure 5. This is difficult but possible for the first generation of hairpin packets generated close to the wall (Adrian & Liu 2002), but it is far more difficult for larger hairpin packets that have undergone many vortex interactions that complicate the shape while growing larger. Further, the vorticity in the hairpins presumably weakens as their scale increases, and we do not have good methods of recognizing weak vortices in the presence of smaller-scale stronger vortices. Without strong proof that the realizations of large-scale motions coincide with mature hairpin packets, we can only conclude that the realizations of large-scale motions in the pipe flow have several properties that are consistent with hairpin packets.

5. Streamwise–azimuthal organization of conditional structures

This section explores the mean structure of the flow around the low-speed streaks of the VLSMs using conditional averages (which are also approximated by LSE), two-point spatial correlations and POD.

5.1. *Conditional average: general u' event and two-point correlation*

For events specified as specific streamwise velocity fluctuation u' values at a point in space, the conditional average of the fluctuating velocity field (u_j') on an x–θ cylinder of radius $r = R - y$ (not explicitly indicated in the equations) is denoted by $\langle u_j'(x', \theta') \mid u'(x, \theta)\rangle$. This field can be approximated by obtaining an LSE as

$$\langle u_j'(x', \theta') \mid u'(x, \theta)\rangle \approx \frac{\langle u'(x, \theta) u_j'(x', \theta')\rangle}{\sigma_u^2} u'(x, \theta), \tag{5.1}$$

in which σ_u denotes the r.m.s. value of $\sqrt{\langle u'^2\rangle}$ (e.g. Adrian 1996; Tomkins & Adrian 2003). The expression on the right-hand side of (5.1) is closely related to the two-point correlation coefficient, which, for the streamwise velocity component, is

$$R_{uu}(\Delta x, \Delta\theta) = \langle u'(x, \theta) u'(x + \Delta x, \theta + \Delta\theta)\rangle / \sigma_u^2, \tag{5.2}$$

where spatial shifts from the event to x' and θ' are represented by Δx and $\Delta\theta$. Thus, the LSE is simply a scaled version of the two-point correlation or the two-point correlation coefficient R_{uu}. (Figure 6 in the x–y plane, which is equivalent to the x–r plane, may be interpreted with an LSE of the streamwise velocity fluctuation given a streamwise velocity fluctuation event, but in this section the estimation is applied in x–θ cylinders.)

A number of other studies have analysed streamwise–spanwise planes in describing turbulence structure. One with the particular focus of understanding long wavering superstructures of streamwise velocity and their effects is Hutchins & Marusic (2007*a*). They found that R_{uu} correlations for turbulent boundary layer measurements were characterized by streamwise-elongated positive correlation regions flanked in the spanwise directions by similarly elongated negative correlation regions, which reflected the striped nature of high- and low-momentum regions near the log layer. Using lower levels of two-point correlation from hot-wire rake experiments, they noted

a distinctive X pattern in the two-point correlation R_{uu}. They constructed synthetic velocity streaks that displaced in the spanwise direction as long-wavelength streamwise sinusoids to show that wavering of the superstructure streaks could cause this feature. This supported their observation that 'the very long features in the log region meander appreciably'.

Other studies shed indirect light on the structure of VLSMs. Ganapathisubramani, Clemens & Dolling (2006) found that two-point correlation results indicated parallel negative u' correlation streaks separated from the positive streak by 2δ spanwise distance in a supersonic turbulent boundary layer flow. At their high Reynolds number of $Re_\tau = 5600$, the positive correlation streak persisted at a correlation coefficient value of $R_{uu} = 0.1$ for streamwise separations of $\pm 6\delta$ and greater than $\pm 8\delta$ for wall-normal locations of $y/\delta = 0.16$ and 0.45, respectively, where δ is boundary layer thickness. They found that the results were consistent with the hairpin vortex packet model (Adrian *et al.* 2000) and the VLSM model of organized packets (Kim & Adrian 1999). Volino *et al.* (2007) studied two-point correlations in streamwise–spanwise planes of turbulent boundary layers over both smooth and rough walls at $Re_\tau = 1772$ and 2438, respectively. For both cases, they also observed parallel, streamwise-oriented, spanwise-offset regions of negative correlation in streamwise velocity correlations R_{uu} at the wall-normal locations of $y/\delta = 0.1$ and 0.4. Additional parallel regions of positive and negative correlation repeated at greater spanwise separations, with low correlation levels. They concluded that these indicated 'a regular spacing of high- and low-speed regions' and attributed the relatively weak correlations of these regions to variation in the streak spacings. The measurement plane limited the streamwise separations to $\pm 2\delta$, and the contours for both the primary correlations and secondary regions frequently appeared to occupy this length.

Delo, Kelso & Smits (2004) used two-point correlation of a passive scalar (smoke in a visualization) to investigate structure in a low-Reynolds-number ($Re_\tau = 300$) turbulent boundary layer. Unlike many other studies, they did not average over multiple realizations or times but only used individual realizations when computing the autocorrelation. Their results revealed diagonal orientations for correlation maxima corresponding to organization of large-scale structures, particularly when far from the wall. At the upper regions of the order of the boundary layer thickness, where unentrained flow existed, unlike the pipe presently being studied, they found structures oriented at very large angles relative to streamwise, but typically within $\pm 50°$. Frequently, multiple diagonal orientations were detectable, which they attributed to multiple diagonal groupings of structures within the spatial extent of the scalar images. At $y/\delta = 0.743$, they found primary orientations of the structures within a narrower range of $\pm 10°$, and this narrowed further to almost a streamwise orientation as the wall was approached, with presumably better converged spatial averaging due to more of the smaller structures occurring within the plane. They observed that groups of large-scale structures often formed agglomerations up to 5δ in length, primarily in the outer portion of the boundary layer.

Elsinga *et al.* (2010) used two-point correlation of swirling strength λ_{ci} to investigate the streamwise–spanwise organization of vortices in a supersonic boundary layer. Their results supported streamwise alignments of hairpins associated with very long low-speed motions, but they also found evidence that hairpins are organized diagonally in the flow, most convincingly when filtering was applied. Hutchins *et al.* (2011) calculated conditional averages with attention given to the wavering of structures and skin friction events. Their results showed meandering to be a prevalent feature of events associated with superstructures.

5.2. *Conditional average: general u' event and two-point correlation results*

Two-point correlations R_{uu} for a series of y positions are displayed in figure 7. The overall features of a strong, streamwise-elongated positive correlation streak for x displacements of the order of several R flanked by spanwise-offset streaks of negative correlation (strongest for small streamwise displacement) are consistent with the previously described results from other wall-bounded turbulent flows. The plots in figure 7 have contour levels chosen to clearly display low-level correlations. As shown by figure 1, u' fluctuations contain many fine scales that would be expected to lose correlation with small spatial displacements. This is also apparent from figure 15(*b*) of Wu *et al.* (2012), in which the total turbulent kinetic energy in u' for $y^+ = 101$ is reduced to 19 % of the unfiltered value when a filter is applied that removes the fine scales to only include very large-scale motions by retaining only the Fourier modes with $\lambda_x \geqslant 6R$ and $\lambda_\theta \geqslant 0.4\pi$. These observations suggest that, given a strong velocity fluctuation event, the average fluctuation strength would decay rapidly with displacement, but more rapidly for azimuthal displacement than streamwise displacement due to the commonly streamwise-aligned and streamwise-elongated form of the fluctuations. Figure 7(*e*) plots the two-point correlation R_{uu} as a surface, and this presentation clearly shows the rapid decay at small separations. Therefore, if one wishes to focus on the larger scales of motion and their correlation, it is necessary to focus on smaller correlation coefficient values, since much of the correlation is associated with the smaller motions. For this reason, figure 7 includes lines at contour levels ranging up to correlation coefficient magnitudes of only 0.05. Colour contours in the region of small displacements are highly saturated.

Figure 7 indicates distinctive patterns of streaks in low levels of the two-point correlations. The streaks have long streamwise extents and are inclined in an azimuthal sense from the streamwise direction with characteristic angles. The most straightforward interpretation of this behaviour is provided by the LSE introduced above, indicating that, on average, this is the pattern of the streamwise fluctuation given a u' fluctuation event. Clearly, instantaneous velocity fields fluctuate about the conditional mean field, and the spike of velocity near the event indicates a great deal of small-scale randomness. But, the length scales of the low-level correlation patterns suggest that they are associated with very long motions. While the small scales may contain much randomness, their form and organization may be strongly influenced by the large scales of motion, as the work of Mathis, Hutchins & Marusic (2009*a*) suggests.

The patterns shown in figure 7 depend somewhat on the sets of velocity fields included in the averages since they are not fully converged. The features near the centre (small displacements) are very consistent even without a high degree of statistical convergence, and the overall character of the patterns at large displacement remain the same. In addition, as is shown in § 6, experiments also provide evidence of the correlation patterns that occur at large $\Delta\theta$ on the other side of the pipe ($|\Delta\theta| > 90°$) when Δx is zero.

The effect of the sign of the u' fluctuation event remains to be considered. The LSE, corresponding to the two-point correlation, necessarily has the same pattern given either positive or negative fluctuations, except that the signs of the velocities in the pattern are reversed. Comparing the results for positive and negative u' events, Lee & Sung (2011) observed the same behaviour in conditional two-point correlations in streamwise–spanwise planes of a turbulent boundary layer simulation, except that there was slight streamwise biasing in different directions based on the signs. For instantaneous streaks in the present pipe flow, it appears that the negative streaks are,

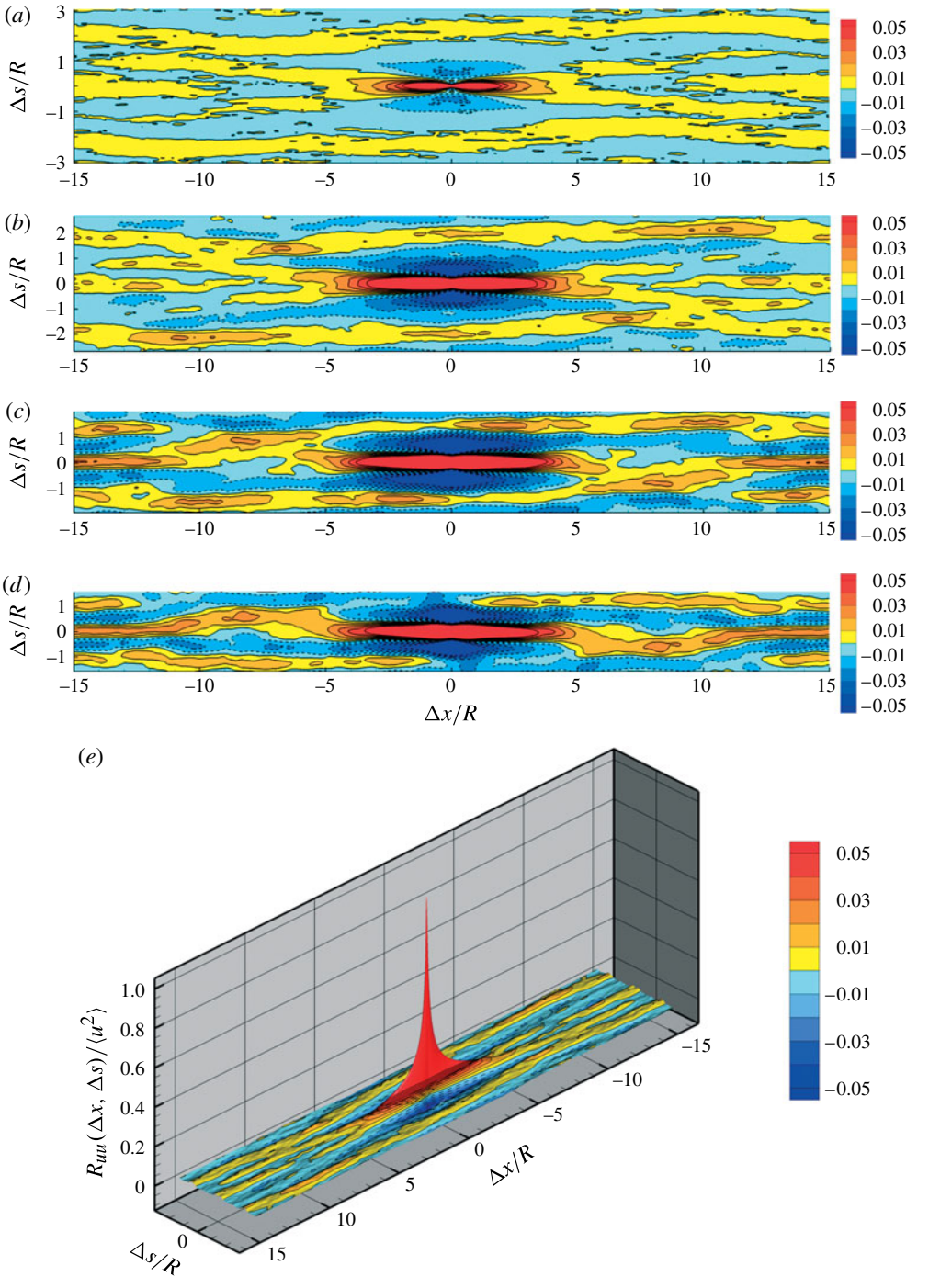

FIGURE 7. Contours of two-point correlation coefficient $R_{uu}(\Delta x, \Delta s)$ in x–θ cylinder surfaces: (*a*) $y^+ = 20$ ($y/R = 0.03$), (*b*) $y^+ = 101$ ($y/R = 0.15$), (*c*) $y^+ = 250$ ($y/R = 0.37$), (*d*) $y^+ = 342$ ($y/R = 0.50$), and (*e*) $y^+ = 80$ ($y/R = 0.12$).

on average, slightly stronger and slightly narrower azimuthally than positive streaks. Since negative streaks are also of interest because of their close relation to structures resembling hairpin packets, they therefore contain appropriate events upon which to focus.

5.3. *Conditional average on long negative u' regions*

The streamwise velocity fluctuations considered in § 5.2 are not very specific events. They could be associated with any point along a high- or low-speed streak. To make the analysis more specific, we consider the conditionally averaged velocity field around a point located at the centre of an instantaneous streak. This quantity is found by locating the centres of long streaks of negative u', shifting the velocity fields such that all centres coincide, and averaging the surrounding fields.

The events are chosen as the centres of mass of the contiguous negative u' streaks extracted in § 3. Only streaks longer than $2R$ are included for specifying events. At the chosen threshold of $u'_{thr} = -0.10U_{bulk}$, an average of 10 such events ($2R$- to $5R$-long clusters) occur per field. Motions of these lengths are generally seen as concatenations of smaller motions, as discussed above, but they are often relatively straight, in the sense of not changing azimuthal inclinations relative to the streamwise direction, although they may be inclined in this manner at constant angles. Since a long streak with such azimuthal inclination appears in three-dimensional space as a helix, the angle relative to streamwise in an x–s plane is referred to henceforth as the *helix angle* to distinguish this angle from that of wall-normal inclination pertaining to structures. Helix angles may be signed positive and negative based on whether s increases or decreases with increasing x, and these correspond to clockwise and anticlockwise rotation of the helices when viewed looking down the positive x axis.

In figure 8(a), the conditional average on long negative u' streak centres is compared to the LSE in (5.1), which estimates the velocity field for a much more general condition of u'. The agreement in the locations of the streaks and locations at which signs change is very good, as indicated by solid lines enclosing red contours and dashed lines enclosing blue contours. Since the LSE in (5.1) is simply proportional to R_{uu}, this is a strong indication that the two-point correlation, even at low levels, contains strong imprints of the patterns of the relatively long regions of negative u' fluctuations.

The features of both the two-point correlation and the conditional average of low-speed streak centres include X-like patterns of positive correlation extending from the location of zero displacement and long, azimuthally inclined, streaky regions of positive and negative correlation at larger displacements. Streaks with similar helix angles are present in instantaneous u' field realizations (figure 1). Dominant helix angles of the relatively low level contours of conditional average (and therefore two-point correlation) are indicated by a solid line in figure 8(a), extending from the zero-displacement region downstream with a helix angle of 5.0°. The line offset azimuthally above the zero-displacement region has a helix angle of 4.2°. It appears that these helix angles may be an imprint of dominant helix angles for structures present in the flow, and this issue will be explored in further depth.

Owing to statistical homogeneity of the flow in the streamwise and azimuthal directions, the autocorrelation must exhibit reflectional symmetry about the origin: $R_{uu}(\Delta x, \Delta s) = R_{uu}(-\Delta x, -\Delta s)$. The property is clear in figures 7 and 8, even though the statistical estimates of R_{uu} are not fully converged. In addition, on physical grounds one expects no preference for structures in the pipe to prefer clockwise or anticlockwise orientations in the long-time average, implying reflectional symmetry

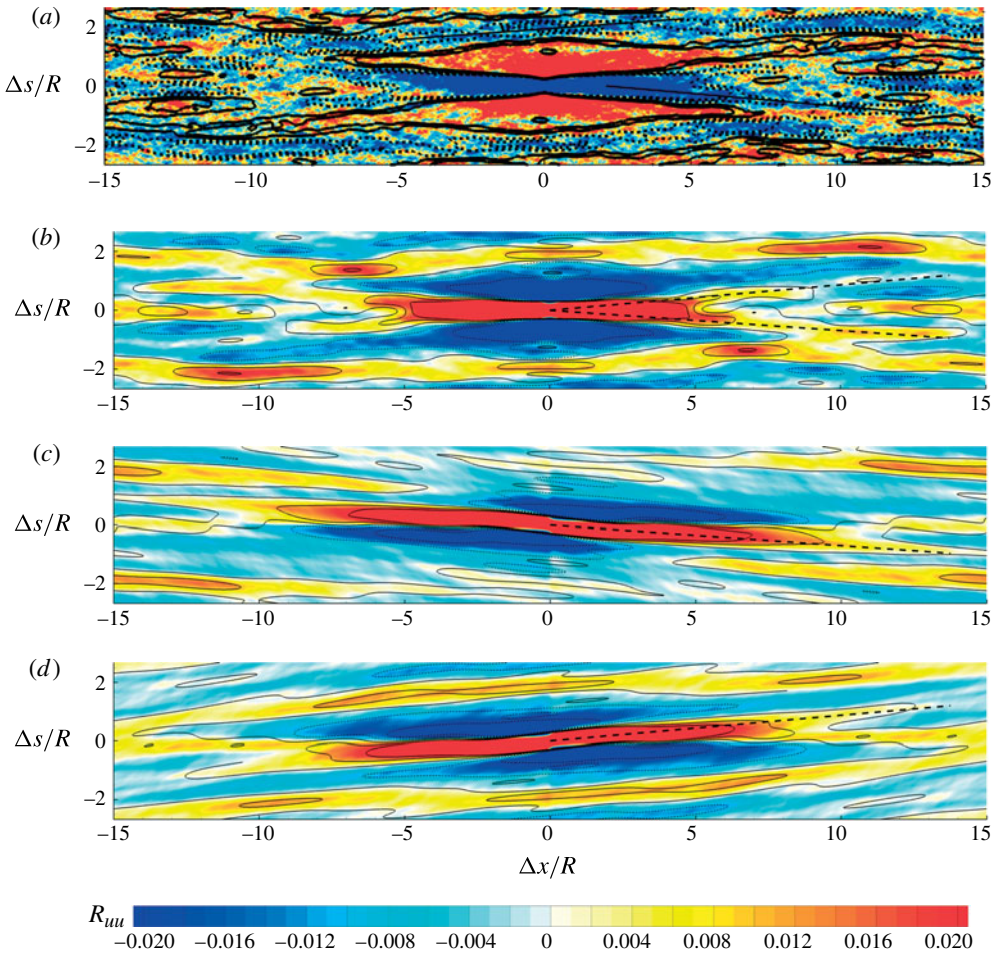

FIGURE 8. (*a*) Conditional average of streamwise velocity fluctuation u' conditioned on events of centres of contiguous regions of negative u' with lengths between $2R$ and $5R$ at $y^+ = 101$ are displayed as colour contours. The LSE for a general negative u' event is plotted with solid black contour lines representing 0.005 and 0.01 of the event strength and dashed black lines representing levels of -0.005 and -0.01. Thick, straight black lines indicate dominant correlation helix angles of approximately 4–5°. (*b*) Two-point correlation with colour contours, with signing unchanged such that red indicates positive correlation. This correlation is decomposed into the two helix angle directions, (*c*) negative and (*d*) positive. In panels (*b–d*), black contour lines (thin dotted for negative) depict the autocorrelation of the low-pass Fourier-filtered u field, retaining streamwise wavelengths of $3.33R$ and arc wavelengths of $0.59R$ (40°) and longer. Levels correspond to 0, 0.01 and 0.02 of the unfiltered correlation magnitude. Thick dashed lines indicate the helix angles of the correlation, 4° in panel (*c*) and 5° in panel (*d*).

of R_{uu} with respect to the $\Delta s = 0$ line. This property is only approximately obeyed in figures 7 and 8 owing to incomplete convergence to the infinite-time average. The deviation from this symmetry provides a clue about the structure. Specifically, the preponderance of structures with positive helix angles (azimuthally inclined towards positive Δs) in figure 7 suggests that the infinite-time symmetry is composed of equal

amounts of structures with positive and negative helix angles, while finite-time average correlations may show a preponderance towards one or the other direction. Hence, the symmetry of the autocorrelation should not be interpreted to imply symmetric structures. In the next section we consider breaking this somewhat artificial symmetry of the statistics by separating the velocity field in x and θ into two contributions containing structures with positive and negative helix angles.

5.4. *Helical features in the two-point correlations and instantaneous u′ fields*

Owing to the periodicity in both the streamwise and azimuthal coordinates, the pipe flow is naturally described by Fourier decomposition in these directions. In the two-dimensional Fourier decomposition, the helix angle sign (direction of rotation) for streaks appearing in each mode is determined by the signs of the wavenumbers k_x and k_θ.

The two-point correlation of the total u, velocity field (the sum of each field decomposed into positive and negative helix angle components) for $y/R = 0.15$ is reproduced in figure 8(*b*). Concentrating on the low-level contours, the X shape noted by Hutchins & Marusic (2007*a*) is clearly evident, and the extremities extending from the X are approximated by dashed lines. The angles for each line are determined independently (4 and 5°) and only drawn on the $\Delta x > 0$ half because of the symmetry. The correlation is decomposed by helix angle by including only those modes with wavenumber pairs (k_x, k_θ) with signs of $(+,+)$ and $(-,-)$ for figure 8(*c*) and signs of $(+,-)$ and $(-,+)$ for figure 8(*d*). That is, figure 8(*c*) is the correlation of the anticlockwise field, and figure 8(*d*) is the correlation of the clockwise field. The pairs of sign combinations are necessary to obtain a real-valued correlation. Computationally, the negative wavenumbers correspond to wavenumbers above the Nyquist wavenumber when taking the discrete Fourier transform (DFT), since DFT coefficients are periodic in wavenumber. In a one-dimensional DFT of a real signal, conjugate symmetry establishes the relation between positive and negative wavenumbers. In the two-dimensional case, the pairs of wavenumber signs correspond to phase relations for the wavenumbers in each coordinate direction. For each mode in physical space, to maintain a constant value of $\mathrm{e}^{\sqrt{-1}(k_x x + k_\theta \theta)}$, and hence a constant value of $k_x x + k_\theta \theta$, x or θ must decrease as the other variable increases for a (k_x, k_θ) wavenumber pair with signs of $(+,+)$ or $(-,-)$. Conversely, x or θ must also increase as the other variable increases for a $(+,-)$ or $(-,+)$ wavenumber pair to maintain a constant value of each mode, thereby establishing the travelling direction.

The modes with $k_x = 0$ and $k_\theta = 0$ are included in both sets by splitting them equally between each set. Thus, the correlation of figure 8(*b*) is precisely equal to the sum of those depicted in figure 8(*c*,*d*). Since the correlation computed in Fourier space involves the combination of each Fourier mode computed independently ($\hat{R}_{ij}(k_x, k_\theta) = \langle \hat{u}_i(k_x, k_\theta) \hat{u}_j^*(k_x, k_\theta) \rangle$), it is equivalent to first decompose the velocity fields by helix angles and compute their two-point correlation or to compute the two-point correlation of the full velocity fields (figure 8*b*) and then decompose the correlation in this manner.

The dashed lines in figure 8(*c*,*d*) are copied from panel (*b*) and also follow the azimuthally inclined positive correlation streaks that remain in each contribution. By synthesizing azimuthally inclined velocity streaks, it is readily observed that the two-point correlation is characterized by the same streak helix angle as that of the synthetic velocity. This remains true when the single streaks are replaced with azimuthally parallel sets of similar streaks with alternating signs of velocity that each represent a low-speed streak azimuthally straddled by high-speed streaks – as with the

profile used in the synthesis by Hutchins & Marusic (2007*a*). The agreement of helix angles supports the concept that each contribution of the helix angle sign-decomposed correlation is formed by very large-scale motions with characteristic helix angles, as are observed in instantaneous velocity fields (figures 1 and 2). The lengths of the primary positive correlation streaks in figure 8(*c*,*d*) are noteworthy, extending for positive displacements of approximately $14R$. Analogous to the discussion in § 3 with regard to energy spectra, the relation between the lengths that appear in the correlation and the structure lengths that appear in velocity fields is dependent on the organization of the velocity structures. However, instantaneous u' features of up to $25h$ (channel half-heights) in streamwise length have been identified by Hutchins & Marusic (2007*a*) in channel DNS, although their example could be interpreted as a combination of several straighter (though spanwise-inclined) velocity structures.

In addition to the primary streaks in each contribution when the correlation is decomposed (figure 8*c*,*d*), weaker streaks also exist located at significant azimuthal displacements. Figure 8(*d*) is simplest, with the additional positive correlation streaks parallel to, but directly azimuthally offset from, the primary streak. The azimuthal locations between the positive correlation streaks are occupied by negative correlation streaks of similar helix angle. The varying configurations in the u' fields, including the varying azimuthal spacings between negative and positive u' streaks, would clearly lead to different azimuthal displacements for peak contributions to the negative correlation regions immediately azimuthally offset from the primary positive correlation streaks. This variation could explain the greater azimuthal widths of these negative correlation regions relative to the other streaks and the consequent lack of azimuthal shift invariance to the overall pattern.

The variations in configurations of velocity fields contributing to the not fully statistically converged correlations are probably largely responsible for the differences between the anticlockwise and clockwise contributions in figure 8(*c*,*d*), as they should possess mirror symmetry as a result of the lack of preferred azimuthal directions. Instead, the anticlockwise (negative helix angle) two-point correlation appears to contain parallel-inclined (same helix angle), azimuthally offset positive correlation streaks with streamwise offsets of half the domain length (as opposed to negligible streamwise offset for those of the clockwise contribution). Owing to the streamwise periodicity, the streamwise-offset streaks can be regarded as continuous in the streamwise direction when the periodic extensions are imagined.

In addition, local maxima at various locations along the secondary streaks may be attributed to the lack of full convergence and to favoured positions in the velocity streaks contributing to the correlation. Also, the number of streaks that occur around the pipe circumference varies between velocity fields and varies with streamwise positions within each velocity field. The number of azimuthal periods for positive and negative fluctuation structures in each velocity field must be an integer because of the azimuthal periodicity. However, azimuthal scale growth also occurs on average with increasing y, as indicated by the decreasing numbers of azimuthal periods at significant streamwise displacements in figure 7 (although the number of azimuthal periods in this correlation remains relatively constant for $\Delta x = 0$). Azimuthal scale growth is explored in greater depth in § 6. Thus, the patterns observed in the correlation are a combination of several integer numbers of u' fluctuation azimuthal periods that occur with varying probability distributions for each y. The observations of Delo *et al.* (2004) with regard to the effects of multiple angles in patterns of structures revealed by the correlations are relevant. Whereas Delo *et al.* (2004) focused on correlations of single fields independently, we have chosen to calculate the correlations averaged over fields

at multiple times. The dominant angle in our correlation is therefore determined by an average over all streak angles that exist in the set of fields, whereas the small number of streak angles that exist in a single field make more distinctive individual contributions when the correlation is calculated for that individual field alone. Since the set of velocity streaks appearing within each field are azimuthally inclined by a distribution of helix angles, the specific set of velocity streaks included in the calculated correlation could affect the locations at which the secondary correlation streaks appear and where local peaks appear along these streaks (owing to interference between the particular streaks included in the average to compute the correlation). Nonetheless, the overall character of the patterns in the correlations would be similar regardless of the particular fields (or set of fields) chosen because the streaks behave similarly and are inclined by angles that are fairly consistent, whereas specific details at large azimuthal displacements would vary. With a sufficiently large set of fields, the correlations would be expected to converge, but the present statistical convergence is sufficient to clearly show the qualitative patterns of the streaks at low correlation levels.

While the discussion has focused on decomposing the correlations, similarly decomposing the velocity fields into clockwise and anticlockwise contributions further establishes the importance of the decomposed correlations and the relation between the velocity fields and the correlation patterns. Simply decomposing the velocity fields as was performed for the two-point correlation yields unclear velocity patterns because of the decomposed small scales. The low-level correlation streaks of interest involve relatively large streamwise and azimuthal scales, and these are accurately represented when the correlation is low-pass-filtered to retain only a fraction of the scales. This may be verified by comparing the contour lines displaying the filtered version of the correlation with the colour contours representing the unfiltered two-point correlation in figure 8. By retaining only these same large scales when decomposing the velocity field, the components of decomposed velocity are much clearer to interpret. As with decomposition by helix angle sign (direction), retaining a particular set of Fourier modes for velocity and then calculating the correlation is equivalent to calculating the correlation for full unfiltered fields and then filtering the correlation by retaining the same set of modes.

The example velocity field in figure 9, which has been filtered, retains the long streaks that may be identified in the unfiltered field (figure 1). Dashed white lines drawn on two prominent examples of negative u' fluctuation streaks with characteristic helix angles demonstrate that these features remain after decomposing into clockwise and anticlockwise components. The helix angles of the identified streaks are slightly steeper than those inferred from the two-point correlation, which are understood as an average. The example field displays a range of helix angles for the long streaks, but the longest examples appear to occur commonly at helix angles consistent with the two-point correlation streaks. In their turbulent boundary layer experiment, Dennis & Nickels (2011) identified ‘spines’ along isosurfaces of very long u' motions to identify the lines they follow in a streamwise–spanwise sense. Their results include a distribution of spanwise-inclined streak structures that are relatively straight, but it appears that meandering is more common than in the present pipe flow, possibly as a result of the different flow geometry. In terms of organization of streaks relative to other streaks within the present pipe domain, as is implied by the long parallel streaks that occur in the two-point correlations, a number of different configurations appear to occur in the instantaneous velocity fields, but a pattern consisting of three parallel

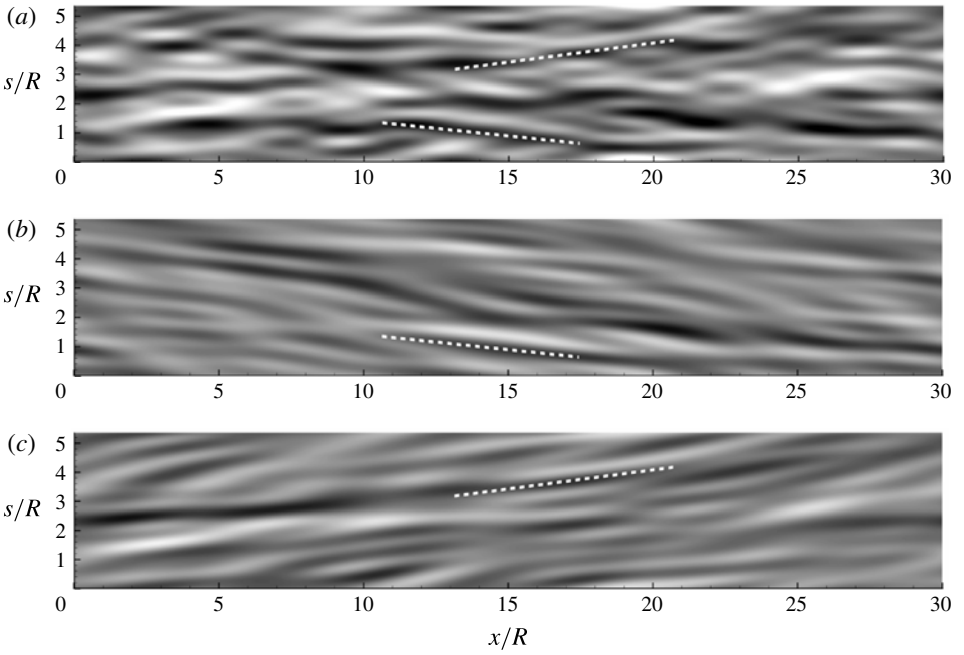

FIGURE 9. (*a*) Filtered version of the u' field in figure 1(*a*), which is decomposed into the two rotation directions in panels (*b*) and (*c*). The filter retains streamwise wavelengths of $3.33R$ and arc wavelengths of $0.59R$ (40°) and longer, which is the same as in figure 8. The example dashed lines (with helix angles of 6.0° in panel (*b*) and 7.5° in panel (*c*)) demonstrate that the associated azimuthally inclined, low-speed (black) streak features are also discernible in the field of panel (*a*) prior to this decomposition.

azimuthal periods of streaks for each rotation direction (helix angle sign) appears conceivable as a common or preferred overall organization for the radius examined.

The overall pattern of the low-level streaks in the two-point correlation can therefore be understood as an imprint of the VLSMs in instantaneous velocity with helix angles of 4–8° and often very long streamwise extent. The secondary streaks centred at azimuthal displacements represent the overall effects of the organizations of these VLSMs, and the secondary streaks may result from the interference patterns created by a combination of the most common configurations. Configurations more frequently included in the finite set of fields averaged would bias the two-point correlation towards their particular associated patterns. These observations are most readily seen when the u' fields and correlations are decomposed by helix angle direction. The pattern of the very long motions represented in the full two-point correlation therefore is dominated by the X pattern created by the dominant clockwise and anticlockwise azimuthally inclined streaks with favoured helix angles. The additional azimuthally inclined regions at greater azimuthal and streamwise displacements may be understood as interference patterns from the more simply described clockwise and anticlockwise components. The combination of helical modes is analogous to McKeon & Sharma (2010) adding helical modes for velocity of opposing azimuthal rotation that have a similar form (not considering radial variation) to the present correlation functions when considering each helix angle separately. McKeon & Sharma (2010) found that adding such modes yielded a pattern of alternating low- and high-speed

streamwise-aligned regions. This was also discussed by Hellström *et al.* (2011). In the present u' correlation, local maxima along the non-primary streaks occur with lengths approximately in the LSM range, and these could be viewed as a result of the interference of the clockwise and anticlockwise components or as preferred locations of LSMs in the finite set of velocity fields included in the average. From the correlation at $\Delta x = 0$, it will be noted in § 6 that characteristic regions of positive correlation on the wall opposite the zero-displacement point are also observed in experiments by Bailey *et al.* (2008) and therefore characterize the organization.

Hutchins & Marusic (2007*a*) also discussed the X-shaped correlation and found that a sinusoidally wavering (in a spanwise sense) synthetic u, streak could generate this pattern. As described above, generating synthetic fields also demonstrates that helical structures can generate similar patterns when averaged over many examples with a distribution of helix angles. The additional structures present in arrangements also generate weaker helical correlation streaks at distances beyond the X shape of the positive correlation. In fact, there is a distribution of helix angles for relatively long structures of negative u', and this leads to a complicated pattern that obscures the individual helical modes.

While there is evidence of very long, sinusoidally wavering structures in the hot-wire rake traces of Hutchins & Marusic (2007*a*), it is more difficult to see clear examples of sinusoidally wavering structures with such length in the present pipe simulation. Guala *et al.* (2006) also identified sinusoidal azimuthal wavering of structures in a pipe flow visualization, but the streamwise wavelength was somewhat greater than $2R$ (and in the LSM range), in contrast to the boundary layer wavelengths of nominally 12δ (well within the VLSM range) identified in Hutchins & Marusic (2007*a*). A distinction should be made between streamwise wavelengths defined based on streamwise Fourier decomposition (as in energy spectra) and streamwise wavelengths defined based on the appearance of azimuthal wavering, although a close correspondence is expected because of the expected behaviour along a constant azimuthal position within an azimuthally wavering streak. Examples of long contiguous or almost contiguous structures each with a consistent overall helix angle (particularly when viewed without focusing on the details) are clearly apparent in figure 2. In an experimental hot-wire rake measurement of a turbulent pipe flow, Monty *et al.* (2007) noted that very long streamwise velocity structures (up to $25R$ in length) could rotate about the pipe axis by 180°, and meandering was also observed. The sinusoidal meandering interpretation can be reconciled with the interpretation based on streaks with constant helix angle by recognizing that long regions of approximately sinusoidal wavering can be split into relatively straight azimuthally inclined segments, so it could be difficult to distinguish between the two interpretations. It appears that each scenario can lead to two-point correlation patterns consistent with those observed in actual flows.

5.5. *Interpretation of organization with multiple scales*

While the VLSMs explain the patterns in the lower magnitude levels of the two-point correlation, the characteristics of the higher levels of correlation are also significant to describing the structure of the turbulent flow. The two-point correlation at magnitudes higher than the VLSM levels is characterized by a streamwise-elongated streak that is more streamwise-aligned (as compared to the X shape associated with VLSMs) and is clearly associated with shorter length structures since it appears at short streamwise displacements. In figure 2 it is apparent that the individual shorter motions organized to form VLSMs frequently possess different azimuthal inclinations (helix

angles) than the overall lines characterizing VLSMs. The shorter-scale motions (than VLSMs) in figures 1 and 2 appear to be more streamwise-aligned than the overall structures (VLSMs) that they appear to comprise. This is consistent with evidence from the two-point correlation, in which contour lines for moderate contour levels are strongly streamwise-elongated (which can be observed from figure 7*e*), as opposed to azimuthally wide, as they would appear if they were associated with structures averaged over a significant range of azimuthal inclinations. The pipe flow experiment of Große & Westerweel (2011) also appears to contain many relatively streamwise-aligned shorter motions of streamwise velocity fluctuation.

Based on the multiple scales of u' motions observed in figure 1 and the descriptions of the various scales in the preceding sections, the following organization scenario emerges for the structure surrounding the negative u' fluctuations. Small, intense velocity fluctuations exist that are somewhat random in their shape and precise dimensions. Such fluctuations are frequently located near vortices and seem, in an average sense, to be consistent with what might be expected from a single hairpin vortex, although the associated intense vortices are often complex in geometry. These velocity fluctuations are somewhat streamwise-elongated, and examples of such fluctuations are shown in figure 1(*d*) with lengths of the order of $0.2R$. These velocity motions frequently appear to organize in streamwise series that may be azimuthally inclined, but appear more often to be closely streamwise-aligned (with their nearest neighbours). Examples can be seen in figure 1(*b*,*c*) as the relatively straight and horizontal (i.e. streamwise-oriented) segments of negative velocity fluctuation. The lengths of these entities vary significantly, but regions often appear straight for approximately $1R$ to $2R$. These may be related to the LSM scales originally identified with turbulent bulges in boundary layers (discussed in Wu *et al.* 2012). It should be noted that the approximate lengths of $1R$–$2R$ are based on observations at $y/R = 0.15$ ($y^+ = 101$) in the present pipe flow, which is at the top of the present flow's log layer (though a similar y^+ value might be considered relatively low in the log layer of a higher-Reynolds-number flow). The $1R$–$2R$ lengths do not contradict the lengths of LSMs traditionally defined from wavelengths in energy spectra that inherently require a negative and positive fluctuation (of the Fourier mode) in streamwise succession. The accepted LSM lengths are based on observations in spectra that include a wide range of Reynolds numbers (Kim & Adrian 1999; Guala *et al.* 2006; Balakumar & Adrian 2007). As noted above, examination of the x–y planes indicated the existence of u' ramps, and other features are consistent with packets, but the actual vortices and their organizations visualized in three dimensions appear distorted from the idealized hairpin vortex packet model. Averaged results, such as two-point correlations, support a ramp-like spatial signature characterizing the streamwise velocity motions (figure 6).

While the lengths observed correspond to observations in the present flow simulation at a single Reynolds number, and therefore the scaling of the lengths cannot be investigated, the lengths are consistent with values proposed in relation to the hairpin packet model. It has been established that the strongest motions in the near-wall region (excluding the VLSM footprints) scale in inner (viscous) units, whereas the characteristic LSM and VLSM wavelengths approximately scale in outer units, based on energy spectra (Guala *et al.* 2006; Balakumar & Adrian 2007). At the present Reynolds number, a consequence of the limited scale separation present in the flow is close interaction between the near-wall region (though not directly with the strongest quasi-streamwise vortices) and the relatively thin log layer. By various scenarios, the near-wall region can generate hairpin vortices or spanwise arches (e.g. Schoppa & Hussain 2002) that would grow into the log layer. Marusic & Adrian (2013) proposed

a scenario in which hierarchies of hairpin packets with different scales grow within the log layer, with higher Reynolds numbers accommodating a greater number of packet scales. In the log layer of the present flow, only limited growth of such structures would occur under the packet hierarchy scenario, and the structure lengths would be expected to correspond closely to those of the hairpin packets being generated at the wall. The lengths of velocity structure features observed in the present pipe flow are comparable to the characteristic lengths of hairpin packets forming in the buffer layer proposed by Marusic & Adrian (2013). The $0.2R$ (140^+) lengths of the small, intense, somewhat streamwise-elongated motions observed in the present flow are consistent with the 100–200^+ lengths of low-speed streaks for the forming hairpins near the buffer layer suggested by Marusic & Adrian (2013). The relatively straight and streamwise-oriented series of the $0.2R$-long motions with overall lengths of $1R$–$2R$ (685–1370^+) observed in the present pipe flow are consistent with the 500–2000^+ lengths suggested for earliest hairpin packets formed in Marusic & Adrian (2013). The appearance of these motions as streamwise-aligned series of the smaller scales further supports their identification as packet-like entities. Note that the inner scalings only apply to the young packets forming, whereas outer scaling of the motions described herein would apply to higher-Reynolds-number flows at similar y/R locations in which hierarchies with more scales of packets are present and more significant growth has occurred from the lower extent of the log layer. However, the limited Reynolds number and consequent log-layer thickness do not prevent the present simulation from accommodating VLSMs and large-scale vortical motions (roll cells, to be considered in § 6) that are clearly distinct from the near-wall quasi-streamwise vortices.

In planes drawn from streamwise–azimuthal cylinder surfaces, the packet-like entities appear to concatenate in streamwise succession, as suggested by Kim & Adrian (1999), but frequently there are also azimuthal offsets as they concatenate, analogous to the spanwise offsets of packets suggested by Balakumar & Adrian (2007) in channels and boundary layers. The offsets in the present flow are apparent in figure 2, in which relatively straight regions of typically $1R$ to $2R$ length connect to each other or are closely organized to form regions that are much longer and often azimuthally inclined. Depending on how offsets occur in concatenations of LSMs, the concatenations could result in VLSMs that are azimuthally sinusoidal or straight with favoured helix angles. In the present pipe simulation, VLSMs appearing as azimuthally inclined streamwise concatenations of straight segments of LSM-length motions are visually most common.

The histograms of figure 3 are now interpreted with respect to the structures of different scales. The $1R$- to $2R$-long regions that tend to be streamwise-aligned are identified with LSMs and packet-like entities. When concatenated into VLSMs, they create merged-together, longer, low-speed regions when connected regions stronger than a particular threshold are extracted for creating the histograms. However, the lengths of the contiguous regions associated with these concatenations that themselves are concatenations of the smallest, most intense motions depend on the strength of each such constituent velocity structure, its geometry and precisely how it is oriented with respect to other structures. Owing to these variations, as the threshold for extracting contiguous regions of fluctuation decreases and they coalesce into longer objects, it is difficult to extract clearly delineated scales for each type of motion. The main organization of the LSMs is in streamwise arrangements often with azimuthal offsets. For this reason, as the threshold decreases below the level appropriate for viewing the LSMs distinctly (which varies between each LSM), more and more LSMs coalesce into the VLSM-length structures with characteristic helix angles that remain

relatively constant over the length of each VLSM. This variation in structures is consistent with the relatively broad length histograms that do not show clear peaks and the relatively broad premultiplied energy spectra, in which the peaks approximately indicate characteristic lengths (though the spectra correspond to streamwise oscillation lengths instead of individual positive or negative fluctuation structure lengths).

6. Azimuthal structure and roll cells

The instantaneous fields and two-point correlation data display significant radial coherence for structures of u' fluctuation, but there is also significant azimuthal scale growth as the wall distance increases (radius decreases), consistent with azimuthal energy spectra in Wu *et al.* (2012). Azimuthal scale growth was also observed in the azimuthal two-point correlations, and these issues were explored for pipe experiments by Monty *et al.* (2007), Bailey *et al.* (2008) and Große & Westerweel (2011). While it is clearly evident in the x–θ surfaces that the signs of velocity fluctuation alternate with θ for a given x position, the manner in which the regions of constant sign widen with increasing y is now considered. To this end, we examine the structure of the instantaneous flow field and the correlation functions in the radial–azimuthal plane next.

While vector fields of the r–θ planes of turbulent pipe flows have not been frequently studied, with the prominent exception of Große & Westerweel (2011), analogous y–z planes in turbulent channel simulations have been examined more often. Aside from a number of studies focusing very near the wall, Hanratty & Papavassiliou (1997) studied vector fields in these planes of relatively low-Reynolds-number channel simulations and the fields of conditional averages for the channel flow based on Q2 events (ejections upwards from the wall accompanied by negative streamwise velocity fluctuation). They observed velocity vector patterns of streamwise-oriented vortices near the wall that they termed ‘wall eddies’. They found that the ‘wall vortices appear to induce sheetlike jets that extend over very large regions of the channel’ and observed structures associated with large Reynolds stress extending far from the wall past the channel centreline. More recently, Mito *et al.* (2007) extended similar analysis to an $Re_\tau = 950$ channel simulation and found that large-scale eruptions appeared in y–z planes. They suggested that vortices located outside the log layer lifted fluid upwards.

An example vector field in an r–θ plane for the present pipe simulation is displayed in figure 10. The appearances of this and other examples are qualitatively similar to those in the pipe measurements of Große & Westerweel (2011). Prominent features are radially inward ejections away from the walls, which are often accompanied by negative u' fluctuations (blue) as slower fluid closer to the wall is transported inwards to the core. These regions correspond to Q2 motions in the flow. In the near-wall region, the azimuthal (arclength) scales of these motions are close to the expected $\Delta s^+ = 100$ value for the wavelength of low-speed streaks (Kline & Robinson 1989). These ejections often occur between two azimuthally separated, counter-rotating quasi-streamwise vortex cores, which are also expected to exist in the near-wall region (Johansson *et al.* 1991; Jeong *et al.* 1997). The behaviour of azimuthally alternating regions of u' fluctuations and quasi-streamwise vortices continues up from the wall approximately to the $y^+ = 30$ circle drawn in the figure. The value $y^+ = 30$ is the nominal lower extent of the log law region and near the upper extent of the most intense near-wall quasi-streamwise vortices.

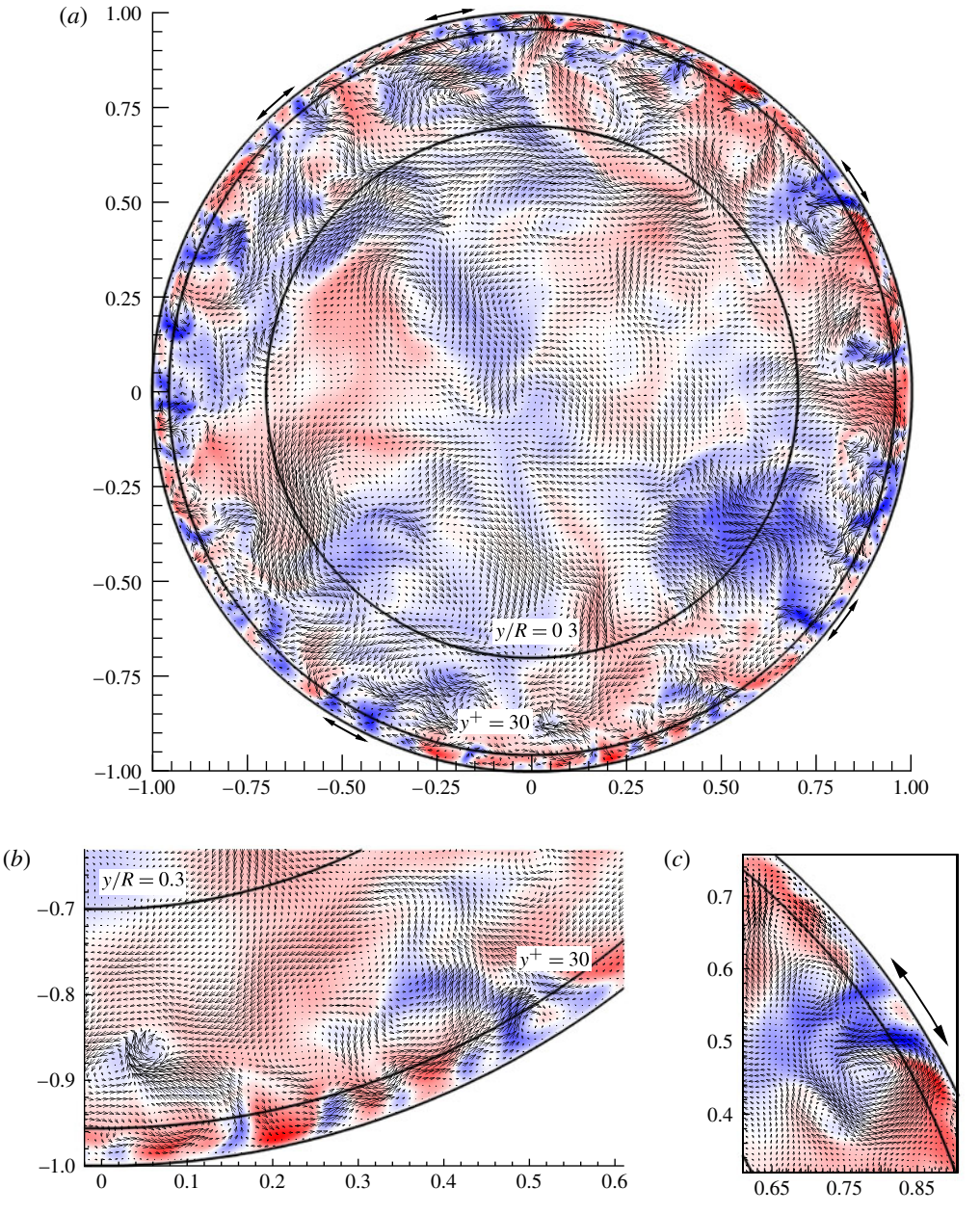

FIGURE 10. Example plane at fixed x position for an instantaneous field of the present pipe simulation showing the in-plane velocity with vectors and the plane-normal velocity (u') fluctuations by colour contours ranging from blue (negative) to red (positive), with presentation similar to Große & Westerweel (2011). (*a*) The entire pipe diameter with vectors interpolated on a coarse uniform grid; (*b*,*c*) details near the walls with vectors on finer grids. Arrows indicate $\Delta s^+ = 100$ arclengths at the wall.

Above the near-wall region, the regions of negative u' fluctuation transported upwards from the wall are observed to merge with increasing y, suggesting that significant azimuthal scale growth is occurring. If the azimuthally wide regions of positive and negative u' fluctuations in the log layer or closely above are followed radially down to the wall, many of the finer motions below these wide regions have a tendency to contain more u' fluctuation of the same sign as the higher-y regions, consistent with the footprints previously observed. It appears that some vortex cores are also oriented normal to this r–θ plane where they intersect. Much of the scale growth (merging) in the instantaneous examples appears to have occurred once y/R values have reached approximately the upper extent of the logarithmic layer. A circle at $y/R = 0.3$ is drawn to indicate a region above the log layer. Elsewhere we have used $y/R = 0.15$ as a nominal upper extent to the log layer (based on the mean velocity profile), but the character of the motions visually changes around $y/R = 0.3$ when viewed from this perspective. The fluctuations above (within) the $y/R = 0.3$ circle appear more isotropic, but tall ejections beginning near the wall are seen to extend above $y/R = 0.3$.

LSEs reveal the average structure associated with a negative u' fluctuation. Instead of calculating a LSE in the x–θ cylinder, as in § 5, this LSE is now computed in the r–θ plane, as Große & Westerweel (2011) also considered. As in § 5.1, the LSE given a low-speed event is simply the scaled two-point correlation of velocity.

In figure 11(*a*), the zero-level contours of the average streamwise velocity fluctuation in a field conditioned on a negative u' event are shown for a series of reference positions y_{ref}. (This plane may be seen in the three-dimensional correlation visualizations in the supplementary material, available at http://dx.doi.org/10.1017/jfm.2012.642, represented by the line contour plane and also the plane that exists at the cuts at $\Delta x = 0$ in these visualizations.) Regions of opposite velocity fluctuation sign that occur azimuthally adjacently on each side of the event are indicated by dashed contour lines. The correlation value of $-0.0004U_{bulk}^2$ corresponds to correlation coefficient values ranging between -0.073 and -0.018, depending on the reference (event) location. The reference locations are indicated by coloured dots, and the contour lines are similarly coloured to identify them with each dot. For the zero-level contours, the lines show a surprising similarity independent of the radial position of the event. These correlation regions are evidence of towering regions of streamwise velocity fluctuation that penetrate deeply into the core while extending outwards far to the wall, consistent with the footprints described by, for example, Hutchins & Marusic (2007*a*) and Mathis *et al.* (2009*a*).

Another noteworthy feature of figure 11(*a*) is the presence of two positively correlated regions on the opposite side of the pipe from the event in the r–θ plane. The correlation lines are relatively independent of the radial locations of the event. These positive correlation regions also correspond to low-speed streaks that would occur in the LSE of a negative u' event, and they are clearly visible in three-dimensional correlation isosurfaces (available in the supplementary material) and the isosurfaces' planar slices at $\Delta x = 0$. These positive correlation streaks observed in this plane provide further description of the azimuthally offset streaks discussed in relation to the x–θ surface contours of figure 7. In experimental two-point correlation measurements of turbulent pipe flow, Bailey *et al.* (2008) also noted the presence of regions of weak positive correlation at large azimuthal separations, of the order of 115°, from the reference position. They found this to support the possibility that VLSMs could be related to nonlinear instabilities that are clearly seen in transition and clearly manifest themselves in that context as coherent structures with periodicity

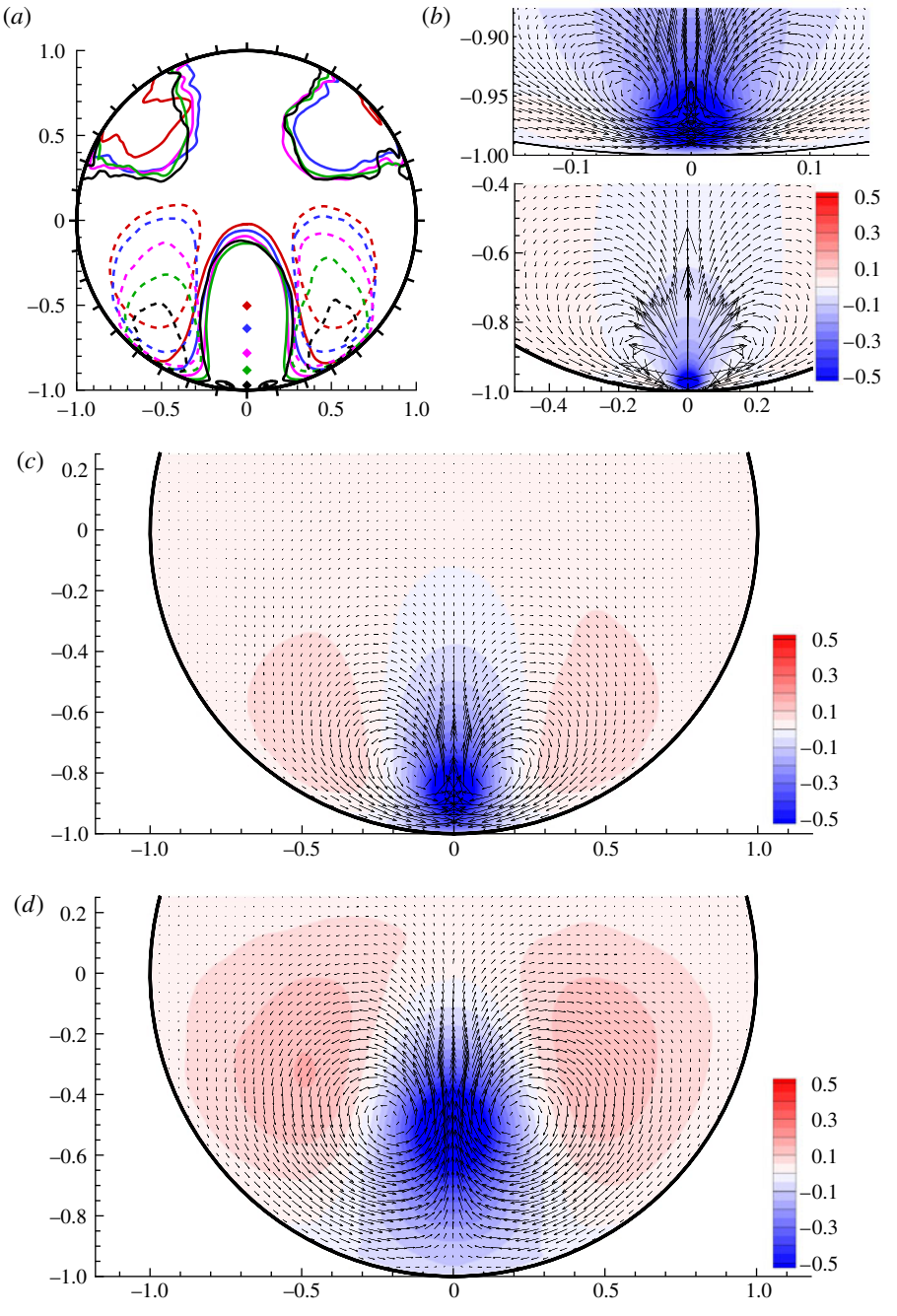

FIGURE 11. (*a*) Contour lines at two-point correlation $R_{uu}(\Delta x = 0, r, r_{ref}, \Delta\theta)$ values of 0 (solid lines) and $-0.0004U_{bulk}^2$ (dashed lines) coloured as the dots indicating the reference points at $r_{ref}/R = \{0.50, 0.63, 0.78, 0.88, 0.97\}$. LSEs of $-u'$ events with colour contours of u' (with levels in 0.05 increments of the event strength) and vectors for the other velocity components are shown for (*b*) $y^+_{ref} = 20$, (*c*) $y^+_{ref} = 101$ ($y/R = 0.15$) and (*d*) $y^+_{ref} = 341$ ($y/R = 0.50$). Panel (*b*) includes an upper part for higher resolution of the event region.

around the pipe circumference (Eckhardt *et al.* 2007). (Note that the colour contours in figure 6 of Bailey *et al.* (2008) display $R_{uu}(\Delta\theta, r)$ in which the only separation is in θ, but this quantity is plotted for a range of radii. Conversely, we display correlation $R_{uu}(\Delta\theta, r, r_{ref})$ for separations in both θ and r in our figure 11(*a*), and a set of r_{ref} values are included.)

Bailey *et al.* (2008) observed the phenomenon of the azimuthally distant regions of positive correlation in their measurements particularly at low Reynolds numbers (for which effects of transition may persist more strongly), such as for $Re_D = 7.6 \times 10^4$. Some weaker positive correlation was also visible at their Reynolds numbers ranging up to $Re_D = 5.5 \times 10^6$. Structures of streamwise velocity in azimuthally periodic arrangements were observed in transitional pipe flows (e.g. Hof *et al.* 2004), and Hof *et al.* (2004) found such structures to agree well with the patterns obtained by extracting travelling waves from a numerical pipe simulation. It is possible that the mechanisms responsible for these motions continue to affect the flow at the present Reynolds number. Hof *et al.* (2004) noted that the waves would probably be unstable in fully turbulent flow, but they potentially could be observable as transients (and thereby leave a statistical imprint). In figure 11(*a*), no positive correlation is discernible above approximately $y/R = 0.3$ in the regions azimuthally offset from the event, based on the contours, which appears consistent with the experimental results of Bailey *et al.* (2008). The presence of these features in both our results and experiment is a strong indication that elements of the patterns observed in the low-level correlations are not merely due to noise, lack of statistical convergence, or streamwise periodicity imposed in the simulation. Note also that we have not imposed azimuthal symmetry in calculating the two-point correlation, and thus the symmetry present is indicative of the degree of convergence of the correlation. Plots of two-point correlation between u' and wall shear stress in Chin *et al.* (2010) for $R^+ = 170$ and 500 pipe flow simulations are suggestive of weak azimuthally offset secondary correlations, but the differences in quantities makes the correlations not directly comparable.

An LSE given a negative u' event may be used to visualize the average velocity in the r–θ plane surrounding a low-speed streak. The in-plane motions are displayed with vectors in figure 11(*b–d*), and colour levels of the contours of the streamwise velocity fluctuation are chosen to represent relatively strong motions, with colours saturating at half the event strength. (The signs of u' are opposite between visualizations of the two-point correlation, such as in figures 7 and 8, and these plots of the LSE, as they are oppositely signed scalings of the two-point correlation for negative u' events.) Independently of the radial location of the negative u' event, a counter-rotating pair of vortices appears centred on the event. The result for the event specified near the wall at $y^+ = 20$ appears similar to structures observed in instantaneous fields such as figure 10, with a pair of vortex cores consistent with legs of quasi-streamwise vortices shown in figure 11(*b*) on a fine-scale grid of vectors. The coarser-spaced vectors in the lower half of figure 11(*b*) display the larger-scale motions in the field for this event, with vector lengths that reveal the weaker motions, and the correlated region of weaker upward ejection and negative u' fluctuation that continues far above the wall. This pattern could be interpreted as a combination of a near-wall motion, between quasi-streamwise vortices, with a weaker contribution extending higher from the wall, perhaps from a footprint of a VLSM. In this scenario, two relatively distinct physical mechanisms would be contributing to this pattern of motion, while the conditional averaging does not distinguish between the effects. The observations of Balachandar & Adrian (1993) for conditional averages in turbulent convection are relevant. Distinct

roll-cell and thermal-plume structures were present for turbulent convection at high Rayleigh numbers, and conditional averages based on the simplest events yielded averages that were superpositions of these two structures. Thus, for the low y^+ event in the present pipe flow, the results do not imply that only a single mechanism is responsible for the flow observed.

For events at higher y values, a somewhat similar pattern in the conditional average also does not necessarily indicate that the same physical mechanisms are responsible for the flow pattern as were responsible for the near-wall event. Furthermore, when asymmetric structures exist that are equally probable to incline in one direction or the opposite direction, the conditional average for a simple event yields a symmetric structure. This appears to be the case for events further above the wall in figure 11(*c*,*d*), where the LSE still indicates qualitatively similar patterns, each with a symmetric pair of vortices, but the instantaneous fields suggest that any such vortices rarely occur in pairs at these distances from the wall. While Balachandar & Adrian (1993) employed multiple event locations to elucidate more information about their flow structures, the present pipe flow three-dimensional fields contain additional information not seen in these planar visualizations and averages that can be exploited using alternative means to relate the patterns of structure to streamwise wavelengths.

One method to analyse the organization of characteristic structures in a flow is POD (Lumley 1967, 1981). Since POD extracts highly energetic structures that may be linearly combined to reconstruct each field and POD is based on the three-dimensional two-point correlation, the POD modes are related to the LSEs of conditional averages. POD was performed in pipe flow at low Reynolds number ($R^+ = 150$) by Duggleby *et al.* (2007), and the present POD methodology is similar. Further details of POD analysis for the present flow are described in Baltzer (2012). The POD analysis is performed using the entire three-dimensional domain and includes all three velocity components with correlation between each component. Owing to the homogeneity and periodicity in x and θ, each velocity component of the POD modes varies trigonometrically as a function of the x and θ spatial coordinates, i.e. the modes are Fourier in those directions. Each mode is assigned a mode number set (i_x, i_θ, n), where i_x and i_θ are indices for which the corresponding mode wavelengths are $\lambda_x = 30R/i_x$ and $\lambda_\theta = 2\pi/i_\theta$. For each (i_x, i_θ) pair, there exists a set of POD modes in which each mode has different radial variations and velocity component behaviours, and n identifies each mode within the set by ordering according to decreasing energy. When i_x and i_θ are both non-zero, the modes take the form of helical waves encompassing all radii (though often with motions concentrated near particular radii), but the modes are otherwise similar in form to the x–θ Fourier decompositions that were performed for individual radii in § 5.4.

The eigenvalues indicate the mean amounts of turbulent kinetic energy that each POD mode contributes to reconstructed fields, so the most energetic modes are particularly important for describing the flow. The $n = 1$ (most energetic) eigenvalues for each streamwise and azimuthal wavenumber index in table 1 include the sum of all Fourier modes with positive and negative wavenumber values for the indices indicated. The eigenvalues therefore represent the contributions of both the clockwise and anticlockwise modes, as well as the complex conjugate mode pairs required to reconstruct a real-valued velocity field. The $n = 1$ modes each account for approximately 90 % of the total energy over all radii (which is equal the sum of the eigenvalues for all n) for each wavenumber pair shown. In table 1, two wavenumber pairs (bold) correspond to particularly energetic modes relative to other wavenumber pairs.

	$i_x = 0$	$i_x = 1$	$i_x = 2$	$i_x = 3$	$i_x = 4$	$i_x = 5$	$i_x = 6$
$i_\theta = 0$	0.0290	0.0599	0.0399	0.0337	0.0240	0.0359	0.0280
$i_\theta = 1$	0.2549	0.4095	0.2074	0.2012	0.1077	0.1864	0.1595
$i_\theta = 2$	0.4757	**1.0132**	0.4656	0.3241	0.1948	0.2028	0.1213
$i_\theta = 3$	0.7464	0.6884	**1.0167**	0.2249	0.2190	0.1134	0.1747
$i_\theta = 4$	0.2813	0.4251	0.3242	0.2316	0.2086	0.1556	0.1252
$i_\theta = 5$	0.2101	0.2681	0.3122	0.3911	0.1575	0.1438	0.1171
$i_\theta = 6$	0.1418	0.1786	0.3396	0.2000	0.1397	0.1380	0.0905

TABLE 1. Eigenvalue spectra of the $n = 1$ POD modes for the pipe flow, displaying the values for the modes with the largest streamwise and azimuthal scales. The two bold eigenvalues correspond to the most energetic modes that are also visualized. The eigenvalues are normalized to percentages such that the sum is 100 if the remaining higher-wavenumber indices are also included along with all modes for higher n.

Figure 12(*a*,*b*) displays the vector patterns in r–θ planes and isosurfaces of u' for these two most energetic $n = 1$ POD modes. The $(i_x = 1, i_\theta = 2)$ mode and the $(i_x = 2, i_\theta = 3)$ mode have helix angles of 5.1 and 6.8°, respectively, at $y/R = 0.15$. The corresponding wavelengths of $30R$ and $15R$ are among the longest VLSM wavelengths that the domain can accommodate. For these particularly energetic POD modes, the helix angles are consistent with those frequently observed for u' structures in the velocity fields and the dominant streaks of the two-point correlations. For a given azimuthal width of u' streaks, which determines the azimuthal wavenumber, the helix angle of a given mode is determined by the streamwise wavenumber. The amount of energy present in these POD modes indicates that modes with these helix angles make sizable contributions to the flow. The mode helix angle at a particular y location is given by $\tan^{-1}[(R - y)2\pi i_x/(L_x i_\theta)]$, where L_x is the $30R$ domain length. It should be noted that the possible helix angles are somewhat coarsely spaced often by several degrees apart, so the angles indicated by the most energetic modes are best understood as corresponding to a range of favoured helix angles appearing in the flow. The angular resolution is sufficient for the most energetic $i_\theta = 3$ mode to be inclined at a steeper angle than the lowest non-zero angle. Dominant helix angles are also observed from instantaneous fields (with figure 9 demonstrating that the very long modes representing the u' motions in figure 1 are clearly represented by the largest-scale Fourier modes) and the two-point correlation (figure 8) to form conclusions in further discussion. The eigenvalue spectra also indicate that significant energy exists in the $i_x = 0$ POD mode for $i_\theta = 3$, suggesting that streamwise-aligned motions with this azimuthal width also make a significant contribution to the flow.

The modes' in-plane velocity vector patterns in figure 12(*a*,*b*) display similarities to the conditional average for an isolated negative u' event. Unlike the conditional average (approximated by an LSE), however, in POD modes the vortices and associated large-scale flow appear in organized patterns periodically around the pipe circumference. The vector pattern remains constant for each POD mode as x varies, except for rotating about the pipe axis in a helical manner. While the anticlockwise modes are visualized, a similar set of clockwise modes also exists for oppositely signed wavenumbers that only varies in that the azimuthal variations are the mirror images of the modes displayed. The overall character of these motions is that of roll cells. While such mode patterns do not typically visually appear symmetrically in the instantaneous planes, particularly as the core is approached, and the addition of other

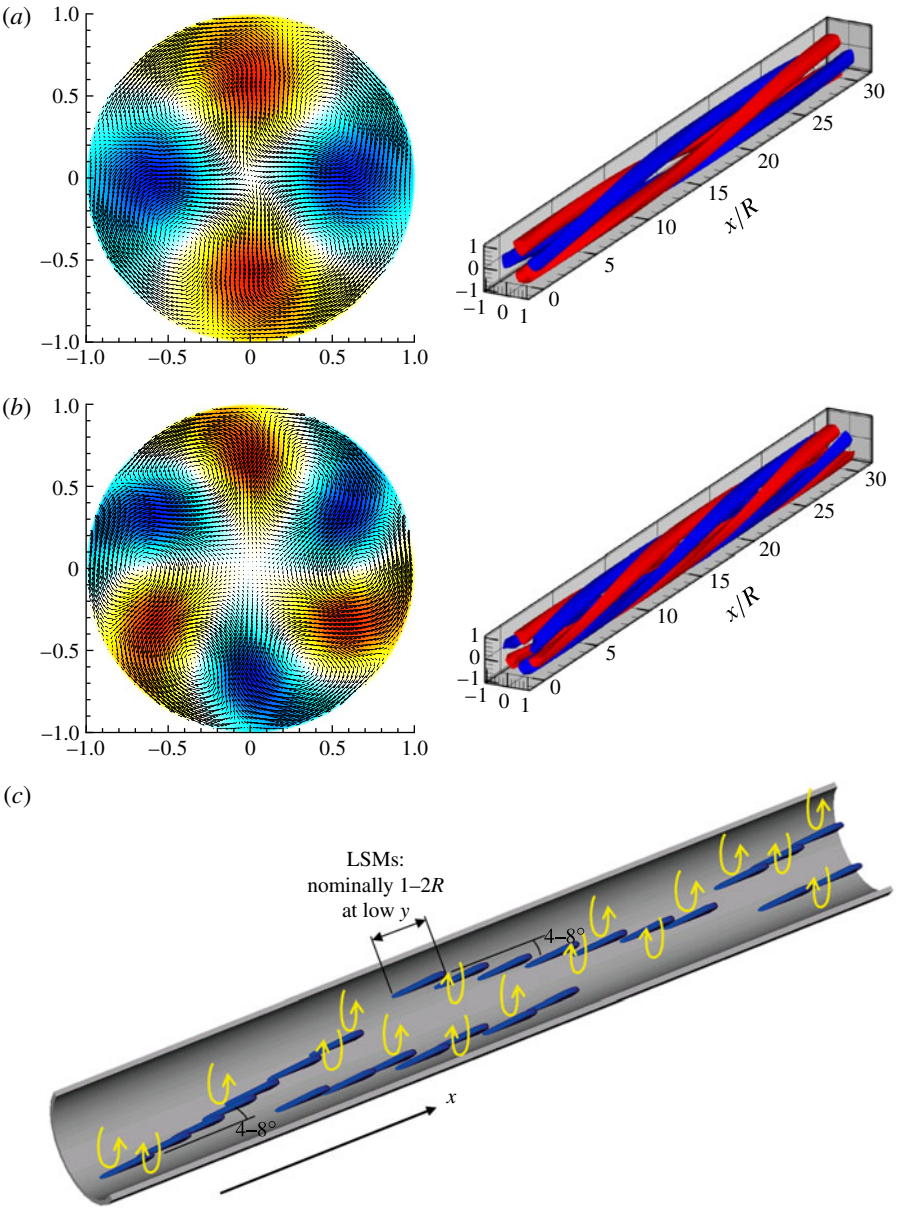

FIGURE 12. The (*a*) ($i_x = 1, i_\theta = 2$) and (b) ($i_x = 2, i_\theta = 3$)$n = 1$ POD modes display roll-cell-like behaviour. The right isosurfaces indicate the swirling patterns of u' (at one-half of maximum magnitude), while the left plots display the colour u' fluctuation and in-plane velocity vectors at $x = 0$ planes. (*c*) An idealized depiction of the organization of LSM-length, ramp-like, relatively straight low-velocity streaks (blue) concatenating following typically azimuthally inclined lines to form VLSMs. Roll cells are schematically represented with yellow arrows indicating axial swirling. High-velocity streaks are omitted and would fill between the motions shown. This figure emphasizes the motions strongly contributing to the log layer, with the smaller (shorter than LSM) scales of motion and the near-wall motions omitted.

POD modes can significantly alter the appearance, the POD modes contain a statistical imprint of an overall roll-cell behaviour in the flow.

Prior studies of wall-bounded turbulent flows have also suggested the presence of roll cells, though much of the discussion has been in the context of turbulent channels. Toh & Itano (2005), in a numerical study of a channel, studied large-scale structures that were in the form of roll cells with counter-rotating large-scale circulations and the interactions of these structures with the near-wall motions. Despite a limited Reynolds number ($Re_\tau = 349$) and the lack of scale separation, they were able to distinguish large-scale motions from the near-wall motions. Performing a stability analysis calculation for an $Re_\tau = 2 \times 10^4$ turbulent channel, del Álamo & Jiménez (2006) show that the two most amplified single-wave solutions with $\lambda_x = 60h$ (channel half-heights) have the form of 'velocity streaks of alternating signs flanked by a pair of counter-rotating streamwise vortices' when viewed in a y–z plane. However, the first one has spanwise wavelength $\lambda_z^+ = 100$ and the second one has $\lambda_z^+ = 2000$, while both are similar in geometry (when scaled to the similar sizes). del Álamo & Jiménez (2006) noted that, although the former structure is consistent with the well-documented near-wall layer, the latter reaches 'deep into the logarithmic layer' as a 'large-scale global structure'. They also related these motions to the 'conical u streaks surrounded by pairs of counter-rotating streamwise vortices' that del Álamo *et al.* (2006) observed for a conditional average of vortex clusters in the logarithmic region of a channel simulation. del Álamo & Jiménez (2006) also observed agreement between the amplitudes of streamwise and wall-normal velocity components for their most amplified solutions and those of principal POD eigenfunctions when considering $Re_\tau = 1000$ channel flow. Considering an approximation to Blasius boundary layer flow, Farrell & Ioannou (2012) used stochastic structural stability theory (SSST) to study the dynamics of streamwise roll and streak structures. They found that these structures are associated with an instability associated with powerful growth. The global optimal structure in this flow appears as a roll cell with a height of several displacement thicknesses.

Hutchins & Marusic (2007*b*) computed the conditional average of a negative u' event at $y^+ = 150$ ($y/h = 0.16$) in a turbulent channel simulation, and found the result in the y–z plane to indicate that a negative u' superstructure was associated with a 'large-scale counter-rotating roll mode'. Their conditional average flow pattern appears similar to the pattern found by del Álamo & Jiménez (2006) and also similar to that of the similar conditional average in the present pipe (figure 11). Marusic & Hutchins (2008) also observed a large-scale roll-cell structure in a y–z plane from two-point correlations calculated from experimental fields of a turbulent boundary layer. They noted the open question of whether this pattern could be attributed to jittering of small-scale vortices or a separate instability related to the superstructure, as del Álamo & Jiménez (2006) suggested. The former possibility is based on the observation of Balakumar & Adrian (2007) that 'the smoothed field of a concatenation of misaligned hairpin packets would look like a pair of meandering counter-rotating streamwise vortices, whose diameters would be of the order of the height and width of the packets'. Based on large-eddy simulations of turbulent channels, Chung & McKeon (2010) also calculated similar roll-cell patterns in a y–z plane for conditional averages based on large-scale low-speed events, where large scales were extracted by filtering. They also discussed the relationship between the conditionally averaged velocity patterns for small-scale and large-scale flow, each based on a large-scale low-speed event. The small-scale pattern retained a roll-cell character in the y–z plane, so it appeared to strengthen the large-scale contribution.

In pipe flows at lower Reynolds numbers, Duggleby *et al.* (2007, 2009) computed POD modes that possessed a similar roll-cell form to the present results. Their $R^+ = 150$ flow, however, would not be expected to contain strong VLSMs or sufficient scale separation to clearly distinguish dominant roll cells organizing the flow. They classified the mode behaviours according to the mode index pairs. The dominant two modes of our calculation, for which the azimuthal mode number index exceeds the streamwise number index, would be classified as 'wall modes'. They observed that the associated coherent structures stayed close to the wall for these modes in their $R^+ = 150$ pipe flow. The differing domain lengths of the present simulation and theirs leads to a lack of equivalence between streamwise wavenumber indices that would be expected to affect the mode classification criteria. Duggleby *et al.* (2007, 2009) also suggested dynamical mechanisms by which the turbulent flow is sustained. For the present pipe flow, the energetic strengths of the two most energetic POD modes that we have identified as corresponding to roll cells are significantly greater than those of POD modes with neighbouring wavenumber indices. This suggests that they represent dominant physical motions in the flow. In addition to the modes' direct contribution of energy, they are also able to strongly influence the flow by organizing other motions. Studies in other flows suggest that the largest scales of POD modes have a more direct link to physical motions than the POD modes of smaller scales that tend to approach an asymptotic form (Moser 1994; Baltzer & Adrian 2011). This reduced distinctiveness for POD modes other than the dominant two is consistent with the Bailey & Smits (2010) conclusions that VLSMs and LSMs are interrelated, which they based on POD eigenvalue behaviour.

The relatively small fraction of the total flow energy represented by the two strongest POD modes identified (just over 2 %) indicates that other motions are important and the relation between the two most energetic modes and the smaller-scale modes is also important. When interpreting the percentages of turbulent kinetic energy associated with these most highly energetic modes, it is important to note that the percentage is calculated relative to the sum of the fluctuations at all radii filling the pipe volume and much of the turbulent kinetic energy is contributed by much smaller scales of motion occupying the region from the wall through the buffer layer. Thus the motions identified by these most energetic roll-cell-like POD modes contribute much more strongly to the flow throughout the log layer and above, such as the $y/R = 0.15$ ($y^+ = 101$) location that has been examined. The roll cells for the modes in figure 12(*a*,*b*) are centred at $y/R = 0.43$ ($y^+ = 300$) and $y/R = 0.31$ ($y^+ = 220$). These locations are far above the near-wall vortices below $y^+ = 60$ and the POD modes represent distinctly different motions, as the associated streamwise wavelengths also indicate.

The energies associated with the modes are consistent with the observation when reconstructing fields from POD modes that the two highly energetic roll-cell modes must be combined with strong net contributions from other scales of motion to produce the strengths of the negative u' streaks in the instantaneous fields. In the instantaneous fields at $y/R = 0.15$, typical peak strengths of the negative u' streaks are of the order of $-0.25U_{bulk}$ (with small peak regions occasionally stronger than $-0.45U_{bulk}$), whereas the contributions of the $(i_x = 1, i_\theta = 2, n = 1)$ and $(i_x = 2, i_\theta = 3, n = 1)$ POD modes to the field of figure 1 have maximum strengths of $-0.014U_{bulk}$ and $-0.011U_{bulk}$ at $y/R = 0.15$ (when the strongest of the clockwise and anticlockwise modes associated with each wavenumber set are considered).

A set of $n = 1$ modes with wavelengths of the $(i_x = 2, i_\theta = 3)$ mode and longer contains 21 independent modes in total (including separate modes for clockwise and

anticlockwise helices), and this set was compared to the single instantaneous field. The correlation coefficient between the unfiltered fluctuating velocity (u') and the contribution of (or projection onto) this mode set ($\tilde{u}'$) for this field at $y/R = 0.15$ is $\rho_{u\tilde{u}} = R_{u\tilde{u}}/(\sigma_u \sigma_{\tilde{u}}) = 0.26$ (σ denotes r.m.s. value of the relevant quantity). As only very long wavelengths ($\geqslant 15R$) are included in these roll-cell POD modes, this correlation value is consistent with the predominance of VLSM energy in the u component (Wu *et al.* 2012). Since the highly energetic u component is largely responsible for the strength of each overall POD mode contribution, the correlation values for the remaining components also indicate how well correlated the other components are to the streamwise fluctuation streaks. For the radial and azimuthal components, the correlation coefficients are $\rho_{v\tilde{v}} = 0.04$ and $\rho_{w\tilde{w}} = 0.12$, respectively. These correlation values indicate that there is significant correlation between the longest scales of these velocity components in the flow and the roll-cell behaviour accompanying the streamwise velocity streaks that are captured by the set of POD modes (which are dominated by the $(i_x = 1, i_\theta = 2, n = 1)$ and $(i_x = 2, i_\theta = 3, n = 1)$ modes). However, the correlation coefficient values are significantly smaller than the streamwise velocity component correlation coefficient because the smaller scales contribute relatively greater fractions of the radial and azimuthal velocity motions. The $\rho_{w\tilde{w}}$ value is consistent with a significant contribution from the roll cells to the azimuthal velocity while smaller scales clearly contribute most of the strength of the azimuthal motions in the field.

While scales smaller than the roll cells are responsible for much of the strong negative u' peaks, the spatial relationships that cause the smaller scales to strengthen the u' motions of the roll cell are consistent with the hypothesis that the largest scales are composed of concatenations of LSMs, as has been shown by the form of the two-point u' correlations. Wu *et al.* (2012) showed that the largest scales of u' motion of this pipe flow remain correlated with patterns that are clearly recognizable when the flow convects downstream by distances of $7R$, with lower correlation levels persisting considerably longer. The time persistence suggests that roll cells associated with the very long streaks that also influence large volumes would play an important role in the organization of the smaller scales of motion. We have also shown (figure 8) that the largest scales are responsible for the low-level patterns in the two-point correlation, and the prominence of the $(i_x = 1, i_\theta = 2)$ and $(i_x = 2, i_\theta = 3)$ modes suggests that the low-level contour azimuthal pattern is dominated by an interference pattern of $i_\theta = 2$ and $i_\theta = 3$ modes. Their sum would lead to a pattern consistent with the pattern of positive correlations appearing on the opposite wall from the event that are not equally azimuthally spaced in the r–θ plane. That this positioning does not correspond to precisely threefold or twofold symmetry is consistent with the correlation locations reported by Bailey *et al.* (2008). Interpretations of the interaction between the roll cells and intense smaller scales of motion will be considered in the conclusion.

For comparison, the clockwise and anticlockwise pair of helical velocity response modes that McKeon & Sharma (2010) summed were created with streamwise wavelengths of $2\pi R$ and azimuthal wavelengths of $2\pi/10$ rad. Using these values, they visualized the resulting arrangement of VLSM streamwise velocity structures with signs alternating in x and θ (their figure 15). Though for a smaller azimuthal wavelength than those of our two most energetic POD modes, their resulting helix angle of 4.9° at $y/R = 0.15$ is comparable to ours. While they generated a streamwise-aligned arrangement of alternating fluctuations by summing similar helical modes of opposite rotation with equal strengths, in our POD reconstructions the strengths can vary significantly between the clockwise and anticlockwise modes for a given set

of wavenumber magnitudes. For the two most energetic modes in the field we have considered, the strengths can differ by a factor of 2 within each mode pair, leading to the azimuthal inclinations. While the strengths of the coefficients vary with each individual field, the overall energy or eigenvalues should be equal for the positive and negative wavenumber pair because of the statistical symmetry when a large set of fields are used for the POD calculation. It is more difficult to compare our results with the experimental pipe POD results of Hellström *et al.* (2011) because they used the snapshot method to calculate POD modes and the resulting modes are not constrained to precise helical forms. The helical form would be gradually approached with many data samples (snapshots) owing to the homogeneity in x and θ (as the eigenvalue spectra of simpler systems suggest (e.g. Duggleby & Paul 2010)). For the set of data in Hellström *et al.* (2011), the two most energetic modes contain long regions of u' that are streamwise-aligned (helix angle of zero). These regions are arranged in such a manner that the streamwise velocity fluctuations alternate signs with their streamwise and azimuthally offset neighbours, as in McKeon & Sharma (2010). In Hellström *et al.* (2011), the azimuthal wavelengths of the structures are irregular, but the pipe circumference appears to contain 3–5 periods.

A summary of the overall organization of negative u' fluctuations above the near-wall region is depicted diagrammatically in figure 12(*c*), with relatively short ramps representing strong levels of the LSMs (which would extend longer, wider and taller if visualized at weak levels). Finer scales of motion and near-wall motions are omitted. This diagram includes long examples of concatenations with the typical characteristic helix angles, as well as several shorter examples that lack strong azimuthal inclinations but waver on an LSM scale. Arrows represent broad vortical motions based on the form of the two most energetic POD modes that each appear in the form of roll cells separating very long streaks of u'.

7. Conclusions

Analysis of structure primarily in the log layer in the DNS of a turbulent pipe flow simulated by Wu *et al.* (2012) shows that long meandering motions of streamwise velocity fluctuation are composed of smaller motions. The following observations focus on $y/R = 0.15$ ($y^+ = 101$ for this flow) at the upper extent of the log layer that is furthest from the direct effects of the near-wall region quasi-streamwise vortices. The motions of streamwise velocity have been divided into three distinct types: short scales of less than approximately $0.2R$ in streamwise length (where distinct negative u' motions are visually observed having lengths of the order of $0.2R$); longer scales frequently of approximately $1R$–$2R$; and VLSMs longer than $3R$. While these dimensions are observations from the present pipe flow and are not intended to assert a specific scaling with Reynolds number, the lengths are reported in outer scaling because the motions appear generally consistent with features observed in other studies that approximately scale in outer units (Kim & Adrian 1999; Guala *et al.* 2006). The large-scale motions of $1R$–$2R$ recognized in this study are broadly consistent with the velocity patterns expected to be associated with large-scale hairpin packets, with negative velocity fluctuation regions frequently possessing ramp-like geometry normal to the wall. Additional study of the surrounding vortical structures is necessary to further justify the association with hairpin packets. The nominally $1R$- to $2R$-long negative velocity fluctuation regions identified in the logarithmic layer and regions nearer the wall are consistent with the LSMs previously defined by wavelengths of $0.3R$–$3R$ based on energy spectra over broad ranges of y and Reynolds numbers and

that were also associated with hairpin vortex packets (Kim & Adrian 1999; Guala *et al.* 2006; Balakumar & Adrian 2007). When comparing between the lengths of 1R- to 2R-long contiguous regions and the lengths of LSMs defined in other studies based on streamwise wavelengths in energy spectra, it must be noted that the quantities are defined inherently differently, with contiguous regions of negative u' in contrast to wavelengths of negative and positive u' in streamwise succession.

The LSM-like motions are frequently observed to align in succession, though they often organize with azimuthal offsets between each other. In this way, they create very long motions that are frequently azimuthally inclined and often appear to waver – with each LSM azimuthally offset, instead of the very long-scale wavering with wavelengths of nominally 12δ in Hutchins & Marusic (2007*a*). The organization is consistent with the proposal of Kim & Adrian (1999), with LSMs concatenating to form VLSMs, except that the concatenations occur along preferred azimuthal inclination angles. The longest examples of VLSMs in the present simulation are most commonly azimuthally inclined and relatively straight along helix angles of 4–8° relative to streamwise, although examples that are highly streamwise-aligned (i.e. with helix angles of approximately zero) are also present, but are generally shorter. Statistical evidence of the arrangement is revealed by two-dimensional (streamwise–azimuthal) two-point spatial correlations. The two-dimensional two-point correlations reveal a streamwise-elongated region of high correlation that decays relatively rapidly in x and is associated with the more streamwise-aligned LSMs (at correlation levels lower than the rapid decay associated with the finest scales of motion). The relatively low correlation levels whose patterns remain unchanged when low-pass Fourier filtering is applied are associated with the VLSMs that are characterized by the 4–8° helix angles, particularly for the longest examples. The two-point correlation also indicates the presence of these motions as correlation persists for very long streamwise displacement distances ($>15R$) along these azimuthal inclinations when decomposed by inclination direction. The non-decomposed two-point correlation, which includes both clockwise and anticlockwise helix directions, contains a more complex pattern. A distinct X shape that arises from superposition of the clockwise and anticlockwise helical modes is the dominant feature, and additional weaker peaks appear from the interference between the helical modes.

While we see that VLSMs consist of LSMs arranged to form the helical VLSM patterns, these observations do not explain how the organization occurs. Study of instantaneous r–θ planes, two-point correlations and the most energetic POD modes suggests the presence of roll cells surrounding the low-speed (and high-speed) elongated VLSM streaks. The two particularly energetic POD modes also possess azimuthal inclination angles consistent with the u' streaks. The roll-cell motions associated with these modes are characterized by diffuse vortical motions bounding low-speed streaks associated with radially thick columns of low streamwise velocity (consistent with the concept of footprints in Hutchins & Marusic (2007*a*)) accompanied by radially inward motion from the wall penetrating deeply towards the core. The roll cells identified in the two strongest POD modes are centred significantly above the wall ($y/R = 0.43$ and 0.31) and are distinct from the quasi-streamwise vortices of near-wall motions. While the symmetry that exists in a conditional average is not often seen in instantaneous examples (particularly when far above the wall), the two strongest POD modes suggest that very long structures including such thick columns organized as patterns of roll cells contribute significantly to the overall flow pattern. The strengths of the roll-cell motions indicate that organized smaller scales are responsible for much of the strength of the streaks observed in the flow.

Clarifying the interaction between the dominant roll cells and intense smaller scales would require a dynamical study to evaluate several possible scenarios. The presence of the large roll cells could sweep the small scales and induce the production of new structures in a scenario similar to that devised by Toh & Itano (2005) for turbulent channel flow. Adrian (2007) suggested the possibility that large scales (perhaps in the form of the roll cells described herein) sweep small-scale vortices near the wall in wall-bounded turbulent flows to the stagnation points in the organized pattern of these large-scale vortices. Based on finding the mode shapes of a given scale that are most strongly amplified in the presence of forcing by other modes present in the flow, McKeon & Sharma (2010) found modes that are likely to be dominant structures in the turbulent pipe flow. Hellström *et al.* (2011) noted the modes of McKeon & Sharma (2010) to be similar in form to POD modes in their turbulent pipe flow experiment, which themselves are similar to the roll-cell POD modes of the present flow. Such modes may be the agency that performs the organization of LSMs into VLSMs. As structures grow from the wall, they can be organized from the effects of the larger-scale motions. Mathis *et al.* (2009*a*,*b*) have shown that very large motions in u' modulate the presence of smaller motions, so the presence of roll-cell-like modes could also induce the presence of the smaller-scale motions identified. As the eigenvalues of the POD for the present flow indicate significantly stronger energy content for the two roll-cell-like modes relative to other modes, an independent mechanism is also possible. Such a mechanism could be similar to the modes observed in pipe transition (Eckhardt *et al.* 2007). del Álamo & Jiménez (2006) suggested a mechanism in channels involving most-amplified wave solutions of an instability in which the solutions have a roll-cell form. In addition, a two-way interaction may exist whereby smaller scales force the roll-cell modes (consistent with McKeon & Sharma 2010), and the roll-cell modes in turn organize the smaller scales.

In conclusion, our evidence is consistent with a physical picture in which the longest VLSMs are formed by the concatenation of LSMs along helix lines principally with helix angles of 4–8° relative to the streamwise direction. The agency by which the LSMs organize is not fully determined, but we favour a model in which helical roll cells either sweep the LSMs into alignment along the stagnation zones between cells or trigger the autogeneration (Zhou *et al.* 1999) of smaller hairpin packets that ultimately grow into LSMs organized along the lines of the roll cell uplifting from the wall. The former picture is motivated by earlier observations by Toh & Itano (2005) (described in Adrian 2007), and it is consistent with the helical roll cells found from POD analysis and the modes presented by McKeon & Sharma (2010).

Acknowledgements

The computer program used in this study was developed by the late Dr C. D. Pierce of the Center for Turbulence Research at Stanford. X.W. was supported by the NSERC Discovery Grant and the Canada Research Chair Program (CRC) in Aeronautical Fluid Mechanics. The calculations were performed at the High Performance Computing Virtual Laboratory (HPCVL). Additional computations were performed using the Arizona State University Advanced Computing Center (A2C2) facilities. J.R.B. and R.J.A. gratefully acknowledge the support of the National Science Foundation with NSF Award CBET-0933848.

Supplementary data

Supplementary data are available at http://dx.doi.org/10.1017/jfm.2012.642.

REFERENCES

ADRIAN, R. J. 1996 Stochastic estimation of the structure of turbulent fields. In *Eddy Structure Identification* (ed. J. P. Bonnet), pp. 145–195. Springer.

ADRIAN, R. J. 2007 Hairpin vortex organization in wall turbulence. *Phys. Fluids* **19**, 041301.

ADRIAN, R. J. & LIU, Z.-C. 2002 Observation of vortex packets in direct numerical simulation of fully turbulent channel flow. *J. Vis.* **5**, 9–19.

ADRIAN, R. J., MEINHART, C. D. & TOMKINS, C. D. 2000 Vortex organization in the outer region of the turbulent boundary layer. *J. Fluid Mech.* **422**, 1–54.

DEL ÁLAMO, J. C. & JIMÉNEZ, J. 2006 Linear energy amplification in turbulent channels. *J. Fluid Mech.* **559**, 205–213.

DEL ÁLAMO, J. C. & JIMÉNEZ, J. 2009 Estimation of turbulent convection velocities and corrections to Taylor's approximation. *J. Fluid Mech.* **640**, 5–26.

DEL ÁLAMO, J. C., JIMÉNEZ, J., ZANDONADE, P. & MOSER, R. D. 2006 Self-similar vortex clusters in the turbulent logarithmic region. *J. Fluid Mech.* **561**, 329–358.

AUBRY, N., HOLMES, P., LUMLEY, J. L. & STONE, E. 1988 The dynamics of coherent structures in the wall region of a turbulent boundary layer. *J. Fluid Mech.* **192**, 115–173.

BAILEY, S. C. C., HULTMARK, M., SMITS, A. J. & SCHULTZ, M. P. 2008 Azimuthal structure of turbulence in high Reynolds number pipe flow. *J. Fluid Mech.* **615**, 121–138.

BAILEY, S. C. C. & SMITS, A. J. 2010 Experimental investigation of the structure of large- and very-large-scale motions in turbulent pipe flow. *J. Fluid Mech.* **651**, 339–356.

BALACHANDAR, S. & ADRIAN, R. J. 1993 Structure extraction by stochastic estimation with adaptive events. *Theor. Comput. Fluid Dyn.* **5**, 243–257.

BALAKUMAR, B. J. & ADRIAN, R. J. 2007 Large- and very-large-scale motions in channel and boundary-layer flows. *Phil. Trans. R. Soc.* A **365**, 665–681.

BALTZER, J. R. 2012 Structure and proper orthogonal decomposition in simulations of wall-bounded turbulent shear flows with canonical geometries. PhD thesis, Arizona State University.

BALTZER, J. R. & ADRIAN, R. J. 2011 Structure, scaling, and synthesis of proper orthogonal decomposition modes of inhomogeneous turbulence. *Phys. Fluids* **23**, 015107.

CHIN, C., OOI, A. S. H., MARUSIC, I. & BLACKBURN, H. M. 2010 The influence of pipe length on turbulence statistics computed from direct numerical simulation data. *Phys. Fluids* **22**, 115107.

CHRISTENSEN, K. T. & ADRIAN, R. J. 2001 Statistical evidence of hairpin vortex packets in wall turbulence. *J. Fluid Mech.* **431**, 433–443.

CHUNG, D. & MCKEON, B. J. 2010 Large-eddy simulation of large-scale structures in long channel flow. *J. Fluid Mech.* **661**, 341–364.

DELO, C. J., KELSO, R. M. & SMITS, A. J. 2004 Three-dimensional structure of a low-Reynolds-number turbulent boundary layer. *J. Fluid Mech.* **512**, 47–83.

DENNIS, D. J. C. & NICKELS, T. B. 2008 On the limitations of Taylor's hypothesis in constructing long structures in a turbulent boundary layer. *J. Fluid Mech.* **614**, 197–206.

DENNIS, D. J. C. & NICKELS, T. B. 2011 Experimental measurement of large-scale three-dimensional structures in a turbulent boundary layer. Part 2. Long structures. *J. Fluid Mech.* **673**, 218–244.

DUGGLEBY, A., BALL, K. S., PAUL, M. R. & FISCHER, P. F. 2007 Dynamical eigenfunction decomposition of turbulent pipe flow. *J. Turbul.* **8** (43), 1–24.

DUGGLEBY, A., BALL, K. S. & SCHWAENEN, M. 2009 Structure and dynamics of low Reynolds number turbulent pipe flow. *Phil. Trans. R. Soc.* A **367**, 473–488.

DUGGLEBY, A. & PAUL, M. R. 2010 Computing the Karhunen–Loève dimension of an extensively chaotic flow field given a finite amount of data. *Comput. Fluids* **39** (9), 1704–1710.

ECKHARDT, B., SCHNEIDER, T. M., HOF, B. & WESTERWEEL, J. 2007 Turbulence transition in pipe flow. *Annu. Rev. Fluid Mech.* **39**, 447–468.

EGGELS, J. G. M., UNGER, F., WEISS, M. H., WESTERWEEL, J., ADRIAN, R. J., FRIEDRICH, R. & NIEUWSTADT, F. T. M. 1994 Fully developed turbulent pipe flow: a comparison between direct numerical simulation and experiment. *J. Fluid Mech.* **268**, 175–210.

ELSINGA, G. E., ADRIAN, R. J., VAN OUDHEUSDEN, B. W. & SCARANO, F. 2010 Three-dimensional vortex organization in a high-Reynolds-number supersonic turbulent boundary layer. *J. Fluid Mech.* **644**, 35–60.

FARRELL, B. F. & IOANNOU, P. J. 2012 Dynamics of streamwise rolls and streaks in turbulent wall-bounded shear flow. *J. Fluid Mech.* **708**, 149–196.

GANAPATHISUBRAMANI, B., CLEMENS, N. T. & DOLLING, D. S. 2006 Large-scale motions in a supersonic turbulent boundary layer. *J. Fluid Mech.* **556**, 271–282.

GANAPATHISUBRAMANI, B., LONGMIRE, E. K. & MARUSIC, I. 2003 Characteristics of vortex packets in turbulent boundary layers. *J. Fluid Mech.* **478**, 35–46.

GROßE, S. & WESTERWEEL, J. 2011 Investigation of large-scale coherent motion in turbulent pipe flow by means of time resolved stereo-PIV. In *The Ninth International Symposium on Particle Image Velocimetry (PIV'11), Kobe, Japan*, 21–23 July 2011.

GUALA, M., HOMMEMA, S. E. & ADRIAN, R. J. 2006 Large-scale and very-large-scale motions in turbulent pipe flow. *J. Fluid Mech.* **554**, 521–542.

HAMBLETON, W. T., HUTCHINS, N. & MARUSIC, I. 2006 Simultaneous orthogonal-plane particle image velocimetry measurements in a turbulent boundary layer. *J. Fluid Mech.* **560**, 53–64.

HANRATTY, T. J. & PAPAVASSILIOU, D. V. 1997 The role of wall vortices in producing turbulence. In *Self-Sustaining Mechanisms of Wall Turbulence* (ed. R. Panton), pp. 83–108. Computational Mechanics Publications.

HELLSTRÖM, L. H. O., SINHA, A. & SMITS, A. J. 2011 Visualizing the very-large-scale motions in turbulent pipe flow. *Phys. Fluids* **23**, 011703.

HOF, B., VAN DOORNE, CASIMIR W. H., WESTERWEEL, J., NIEUWSTADT, F. T. M., FAISST, H., ECKHARDT, B., WEDIN, H., KERSWELL, R. R. & WALEFFE, F. 2004 Experimental observation of nonlinear travelling waves in turbulent pipe flow. *Science* **305** (5690), 1594–1598.

HUTCHINS, N., HAMBLETON, W. T. & MARUSIC, I. 2005 Inclined cross-stream stereo particle image velocimetry measurements in turbulent boundary layers. *J. Fluid Mech.* **541**, 21–54.

HUTCHINS, N. & MARUSIC, I. 2007*a* Evidence of very long meandering features in the logarithmic region of turbulent boundary layers. *J. Fluid Mech.* **579**, 1–28.

HUTCHINS, N. & MARUSIC, I. 2007*b* Large-scale influences in near-wall turbulence. *Phil. Trans. R. Soc.* A **365**, 647–664.

HUTCHINS, N., MONTY, J. P., GANAPATHISUBRAMANI, B., NG, H. C. H. & MARUSIC, I. 2011 Three-dimensional conditional structure of a high-Reynolds-number turbulent boundary layer. *J. Fluid Mech.* **673**, 255–285.

JEONG, J., HUSSAIN, F., SCHOPPA, W. & KIM, J. 1997 Coherent structures near the wall in a turbulent channel flow. *J. Fluid Mech.* **332**, 185–214.

JIMÉNEZ, J. & PINELLI, A. 1999 The autonomous cycle of near-wall turbulence. *J. Fluid Mech.* **389**, 335–359.

JOHANSSON, A. V., ALFREDSSON, P. H. & KIM, J. 1991 Evolution and dynamics of shear-layer structures in near-wall turbulence. *J. Fluid Mech.* **224**, 579–599.

KIM, H. T., KLINE, S. J. & REYNOLDS, W. C. 1971 The production of turbulence near a smooth wall in a turbulent boundary layer. *J. Fluid Mech.* **50**, 133–160.

KIM, K. C. & ADRIAN, R. J. 1999 Very large-scale motion in the outer layer. *Phys. Fluids* **11**, 417–422.

KLINE, S. J. & ROBINSON, S. K. 1989 Quasi-coherent structures in the turbulent boundary layer. Part I: Status report on a community-wide summary of the data. In *Near Wall Turbulence* (ed. S. J. Kline & N. H. Afgan), pp. 218–247. Hemisphere.

LEE, J. H. & SUNG, H. J. 2011 Very-large-scale motions in a turbulent boundary layer. *J. Fluid Mech.* **673**, 80–120.

LEKAKIS, I. C. 1988 Coherent structures in fully developed turbulent pipe flow. PhD thesis, University of Illinois at Urbana-Champaign.

LUMLEY, J. L. 1967 The structure of inhomogeneous turbulent flows. In *Atmospheric Turbulence and Radio Wave Propagation* (ed. A. M. Yaglom & V. I. Tatarsky), pp. 166–178. Nauka.

LUMLEY, J. L. 1981 Coherent structures in turbulence. In *Transition and Turbulence* (ed. R. E. Meyer), pp. 215–241. Academic.

MARUSIC, I. 2001 On the role of large-scale structures in wall turbulence. *Phys. Fluids* **13**, 735–743.

MARUSIC, I. & ADRIAN, R. J. 2013 Scaling issues and the role of organized motion in wall turbulence. In *Ten Chapters in Turbulence* (ed. P. A. Davidson, Y. Kaneda & K. R. Sreenivasan), Cambridge University Press.

MARUSIC, I. & HUTCHINS, N. 2008 Study of the log-layer structure in wall turbulence over a very large range of Reynolds number. *Flow Turbul. Combust.* **81**, 115–130.

MATHIS, R., HUTCHINS, N. & MARUSIC, I. 2009*a* Large-scale amplitude modulation of the small-scale structures in turbulent boundary layers. *J. Fluid Mech.* **628**, 311–337.

MATHIS, R., MONTY, J. P., HUTCHINS, N. & MARUSIC, I. 2009*b* Comparison of large-scale amplitude modulation in turbulent boundary layers, pipes, and channel flows. *Phys. Fluids* **21**, 111703.

MCKEON, B. J. & SHARMA, A. S. 2010 A critical-layer framework for turbulent pipe flow. *J. Fluid Mech.* **658**, 336–382.

MITO, Y., HANRATTY, T. J., ZANDONADE, P. & MOSER, R. D. 2007 Flow visualization of superbursts and of the log-layer in a DNS at $Re_\tau = 950$. *Flow Turbul. Combust.* **79**, 175–189.

MONTY, J. P., STEWART, J. A., WILLIAMS, R. C. & CHONG, M. S. 2007 Large-scale features in turbulent pipe and channel flows. *J. Fluid Mech.* **589**, 147–156.

MOSER, R. D. 1994 Kolmogorov inertial range spectra for inhomogeneous turbulence. *Phys. Fluids* **6** (2), 794–801.

PERRY, A. E. & CHONG, M. S. 1982 On the mechanism of wall turbulence. *J. Fluid Mech.* **119**, 173–217.

SCHOPPA, W. & HUSSAIN, F. 2002 Coherent structure generation in near-wall turbulence. *J. Fluid Mech.* **453**, 57–108.

SMITH, C. R. & METZLER, S. P. 1983 The characteristics of low-speed streaks in the near-wall region of a turbulent boundary layer. *J. Fluid Mech.* **129**, 27–54.

TOH, S. & ITANO, T. 2005 Interaction between a large-scale structure and near-wall structures in channel flow. *J. Fluid Mech.* **524**, 249–262.

TOMKINS, C. D. & ADRIAN, R. J. 2003 Spanwise structure and scale growth in turbulent boundary layers. *J. Fluid Mech.* **490**, 37–74.

TOWNSEND, A. A. 1976 *The Structure of Turbulent Shear Flow*, 2nd edn. Cambridge University Press.

VOLINO, R. J., SCHULTZ, M. P. & FLACK, K. A. 2007 Turbulence structure in rough- and smooth-wall boundary layers. *J. Fluid Mech.* **592**, 263–293.

WU, X., BALTZER, J. R. & ADRIAN, R. J. 2012 Direct numerical simulation of a $30R$ long turbulent pipe flow at $R^+ = 685$: large- and very large-scale motions. *J. Fluid Mech.* **698**, 235–281.

WU, Y. & CHRISTENSEN, K. T. 2006 Population trends of spanwise vortices in wall turbulence. *J. Fluid Mech.* **568**, 55–76.

WU, X. & MOIN, P. 2008 A direct numerical simulation study on the mean velocity characteristics in turbulent pipe flow. *J. Fluid Mech.* **608**, 81–112.

ZHOU, J., ADRIAN, R. J., BALACHANDAR, S. & KENDALL, T. M. 1999 Mechanisms for generating coherent packets of hairpin vortices in channel flow. *J. Fluid Mech.* **387**, 353–396.